Moulin density controls the timing of peak pressurization within the Greenland Ice Sheet's subglacial drainage system

Jessica Mejia[1], Jason Gulley[2], Celia Trunz[3], Matthew David Covington[4], Timothy Bartholomaus[5], Charles Breithaupt[6], Surui Xie[7], and Timothy H Dixon[2]

[1]University at Buffalo
[2]University of South Florida
[3]Université de Sherbrooke
[4]University of Arkansas at Fayetteville
[5]University of Idaho
[6]ExxonMobil
[7]University of Houston

November 21, 2022

Abstract

Links between hydrology and sliding of the Greenland Ice Sheet (GrIS) are poorly understood. Here, we monitored meltwater's propagation through the entire glacial hydrologic system for catchments at different elevations by quantifying the lag cascade as daily meltwater pulses traveled through the supraglacial, englacial, and subglacial drainage systems. We found that meltwater's residence time within supraglacial catchments-depending upon area, snow cover, and degree of channelization-controls the timing of peak moulin head, resulting in the two hour later peak observed at higher-elevations. Unlike at lower elevations where peak moulin head and sliding coincided, at higher elevations peak sliding lagged moulin head by ~2.8 hours. This delay was likely caused by the area's lower moulin density, which required diurnal pressure oscillations to migrate further away from subglacial conduits to elicit the observed velocity response. These observations highlight the supraglacial drainage system's control on coupling GrIS hydrology and sliding.

Moulin density controls the timing of peak pressurization within the Greenland Ice Sheet's subglacial drainage system

J. Z. Mejia[1], J. D. Gulley[2], C. Trunz[3], M. D. Covington[4], T. C. Bartholomaus[5], C. Breithaupt[6], S. Xie[7], T. H. Dixon[2]

[1]Department of Geology, University at Buffalo, Buffalo, NY 14260
[2]Department of Geosciences, University of South Florida, Tampa, FL 33620.
[3]Department of Applied Geomatics, Université de Sherbrooke, Sherbrooke, QC J1K 2R1
[4]Department of Geosciences, University of Arkansas, Fayetteville, AR 72701
[5]Department of Earth and Spatial Sciences, University of Idaho, Moscow, ID 83844
[6]Exxonmobil Upstream Research Company, Spring, TX 77389
[7]Department of Civil and Environmental Engineering, University of Houston, Houston, TX 77204

Key Points:

- Larger catchments within the Greenland Ice Sheet's ablation area impart significant delays on the timing of meltwater delivery to moulins
- Peak moulin head occurred 1–3.25 hours later at higher elevations
- Peak moulin head and sliding speeds are not coincident where moulin density is low

Corresponding author: Jessica Mejía, jzmejia@buffalo.edu

Abstract

Links between hydrology and sliding of the Greenland Ice Sheet (GrIS) are poorly understood. Here, we monitored meltwater's propagation through the entire glacial hydrologic system for catchments at different elevations by quantifying the lag cascade as daily meltwater pulses traveled through the supraglacial, englacial, and subglacial drainage systems. We found that meltwater's residence time within supraglacial catchments—depending upon area, snow cover, and degree of channelization—controls the timing of peak moulin head, resulting in the two hour later peak observed at higher-elevations. Unlike at lower elevations where peak moulin head and sliding coincided, at higher elevations peak sliding lagged moulin head by ~ 2.8 hours. This delay was likely caused by the area's lower moulin density, which required diurnal pressure oscillations to migrate further away from subglacial conduits to elicit the observed velocity response. These observations highlight the supraglacial drainage system's control on coupling GrIS hydrology and sliding.

Plain Language Summary

Each summer, melting snow and ice collects within stream and rivers on the Greenland Ice Sheet's surface until reaching crevasses or moulins—near-vertical conduits that penetrate the entire ice thickness—where this meltwater can lubricate the bed, causing the overlying ice to slide more rapidly. Despite the important role of meltwater in modulating sliding speeds, little is known about how relationships between melting and sliding vary spatially or through time. Here, we take the novel approach of monitoring meltwater's propagation through the entire glacial hydraulic system at two elevations. We find that longer delays in the timing of meltwater delivery to moulins draining larger, higher-elevation catchments, caused peak moulin water level (i.e., peak pressurization) to occur two hours later in the day than at smaller, lower-elevation catchments. Unlike at lower elevations where peak moulin water level and sliding coincided, at higher elevations sliding lagged peak moulin water level by 2.8 hours. This delay was likely caused by the fewer number of moulins which require a single moulin to pressurize a larger proportion area. This work reveals the importance of the supraglacial drainage system in imparting controlling the timing of meltwater reaching the bed and its relationship with sliding.

1 Introduction

Accurate predictions of the Greenland Ice Sheet's (GrIS) future contributions to sea level rise require a good understanding of the dynamic links between melting, subglacial water pressures, and ice motion. Meltwater produced on the ice sheet's surface flows through complex networks of supraglacial streams and rivers that ultimately empty into crevasses or moulins (Rennermalm et al., 2013; Smith et al., 2015; Yang & Smith, 2016). Moulins are vertical conduits that penetrate the entire ice thickness and connect to the most efficient parts of the dynamic subglacial drainage system (Gulley et al., 2012). Meltwater inputs to moulins modulate subglacial water pressures and basal traction, which controls sliding (Andrews et al., 2014; Bartholomaus et al., 2007). Accordingly, the supraglacial, englacial, and subglacial drainage systems are inherently linked, meaning that changes in any of these components can impact ice motion. Despite the hydraulic system's interconnections, most studies of glacial hydrological systems have focused on one component at a time, resulting in critical gaps in our understanding of links between changes in hydrology and ice motion.

Large scale ice sheet models exclude key components of the glacial hydrologic system when investigating the ice-dynamic response to melting (Goelzer et al., 2020). Frequently, the supraglacial drainage system is overlooked under the assumption that meltwater delivery to the subglacial drainage system is coincident with peak melting across the ablation area. Such simplifications contrast with observations that reveal significant heterogeneity in the timing of meltwater delivery to moulins (King, 2018; Yang & Smith, 2016; Yang et al., 2018), which can lag peak melting by up to 16 hours for the largest catchments (Smith et al., 2017). Observations show temporal lags between peak melting and peak sliding speeds increase with elevation and distance from the ice sheet's margin (Hoffman et al., 2011), suggesting there should be spatiotemporal differences in the hydro-dynamic coupling throughout the GrIS ablation area. These lags are likely caused by longer delays in the timing of meltwater delivery to moulins with larger catchment areas, which similarly increase with elevation as moulin density decreases (Clason et al., 2015; Yang et al., 2018). Even though the importance of meltwater inputs on sliding is well documented, how differences in the timing of meltwater delivery to moulins and their spatial distribution impact sliding has not been fully investigated.

Here we take a novel and holistic approach to understanding relationships between melting and sliding on the GrIS by quantifying lags in meltwater propagation through each component of the glacial hydraulic system. We established two field camps at different elevations—a lower elevation field camp, Low Camp, and a higher-elevation camp, High Camp—where we measured the timing of daily peaks in melting, meltwater delivery to moulins, moulin hydraulic head (the water level within the moulin with respect to sea level), and surface ice velocity. We use these observations to investigate how differences in the physical characteristics of supraglacial drainage basins control lags between peak meltwater production and delivery to moulins and how these differences impact sliding.

2 Data and Methods

2.1 Field Sites

In July 2017, we established two camps within the ablation area of Sermeq Avannarleq in west Greenland: a lower elevation site *Low Camp* and a higher-elevation site *High Camp* at elevations of 779 and 947 m.a.s.l., respectively (Figure 1; Table S2; Ice thicknesses of 503 and 790 m (Morlighem et al., 2017)). We monitored meltwater propagation within an internally drained catchment at each elevation, the moulins of which we refer to as JEME (at Low Camp), and RADI (at High Camp) (Figure 1b–c). To constrain the timing and magnitude of daily melting we installed an automatic weather station at each camp (Text S4), supplementing our observations with data from the nearby GC-NET station JAR1 (Figure 1; Steffen et al., 1996). We monitored the timing of meltwater delivery to each catchment's terminal moulin using ultrasonic water level sensors positioned approximately 30 m upstream of each moulin (Figures S1–S4). We measured moulin water level by directly instrumenting moulins with pressure transducers, allowing us to monitor pressure fluctuations within the most hydraulically connected parts of the subglacial drainage system. On 21 July we instrumented Low Camp's JEME moulin (69.474°N, -49.825°E) which drained $\sim$0.2 km^2 (Figure 1; Table S1). On 29 July we instrumented High Camp's Radical moulin (RADI; 69.543°N, -49.693°E) which drained $\sim$16.7 km^2 (Figure 1; Tables S1 and S3). Finally, we monitored ice motion by installing several global navigation satellite system (GNSS) stations at both camps (Text S6).

In 2018 we returned to the field to expand our observations. Before the onset of melting, we installed a seismic station to measure glaciohydraulic tremor amplitude, a proxy for the discharge and pressure gradient within subglacial conduits (Text S7; Bartholomaus et al., 2015; Gimbert et al., 2016), within Low Camp's main catchment JEME. On 10 July, we instrumented the newly formed PIRA moulin which drained the same catchment as JEME moulin the previous year (catchment area $\sim$0.2 km^2; Figure S3). PIRA moulin formed in approximately the same location as JEME moulin was before it had advected $\sim$90 m downglacier over the winter. To further constrain catchment area induced delays in meltwater delivery to moulins, we instrumented two auxiliary catchments with supraglacial stream gauges: JNIH catchment at Low Camp (July 2017; area $\sim$1.1 km^2), and SBPI catchment at High Camp (August 2018; $\sim$2.4 km^2; Figure 1).

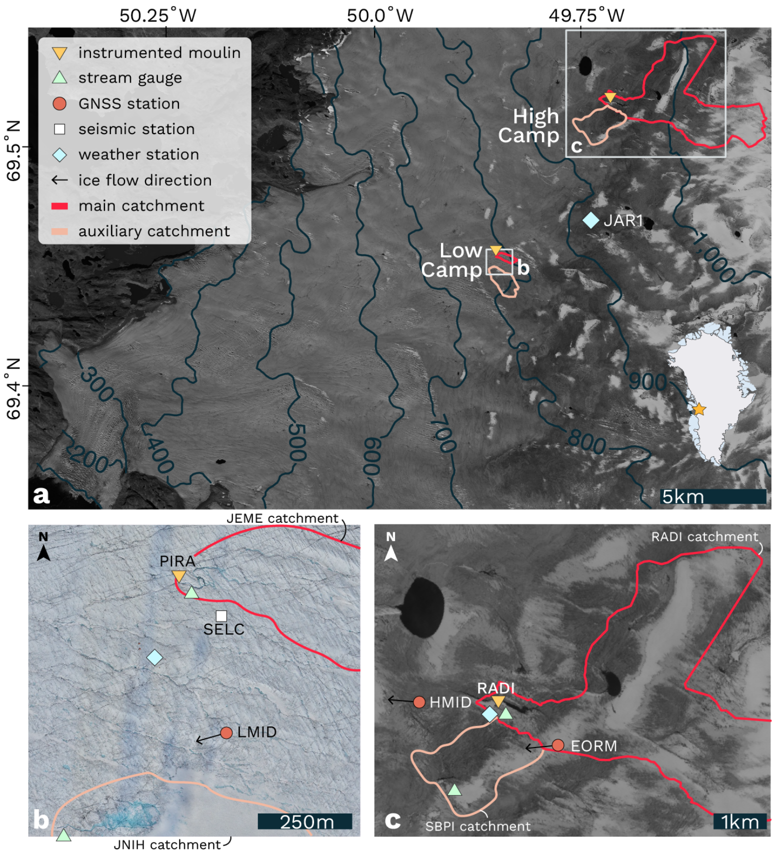

Figure 1. Sermeq Avannarleq field sites. (a) Sentinel-2 imagery from 10 Aug 2018 showing the full extent of the catchments studied at Low Camp and High Camp. (b) July 2018 drone orthophoto showing Low Camp, our main catchment JEME is outlined in red. PIRA (yellow triangle) and JEME moulins draining this catchment were located in the same position in 2017 and 2018 (Figures S1, S3–S4). (c) High Camp zoom in showing instrumented moulin RADI (yellow) with outlined catchment (Figures S2 and S5).

3 Results

The instruments deployed during the 2017 and 2018 melt seasons allowed us to monitor and constrain the timing of meltwater propagation through the glacial hydraulic system for catchments at Low Camp and High Camp. We deployed the first instruments in July 2017 after the melt season had already begun and the snowline had retreated past both our lower and higher-elevation sites.

3.1 Meltwater production

We used recorded meteorological measurements and the enhanced temperature-index model by Pellicciotti et al. (2005) to calculate melt rates to constrain the timing of peak meltwater production (Text S3; Figures 3a, S9a–S11a). Melting peaked simultaneously across our study area (Figure 2), occurring around 13:30±1.4 hours local time (henceforth all times are reported in local time (UTC-02:00). The timing and magnitude of peak melting was most strongly correlated with incoming solar radiation (Text S3). A comparison between calculated melt rate and ice surface ablation recorded at Low Camp (Text S3; 13 July–19 August 2017) shows good agreement with peak ablation occurring 13:30±

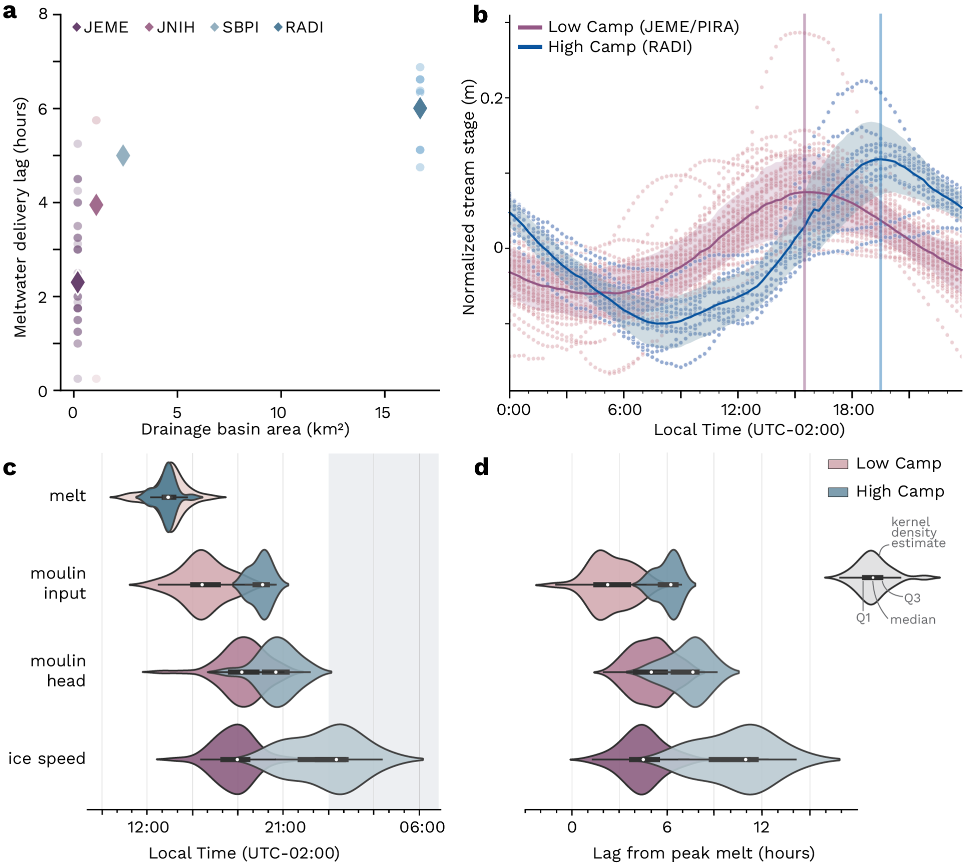

Figure 2. (a) Peak melting to meltwater delivery lag with respect to catchment area. Diamonds mark mean values with dots representing individual observations. (b) Normalized daily supraglacial stream stage for our catchments at Low Camp (purple) and High Camp (blue) primary catchments. The mean timing of diurnal peaks are marked with vertical lines. (c) Box plots overlaid by height-normalized kernel density estimates showing the timing of peak melting, meltwater delivery to moulins, moulin head, and ice speed for Low Camp (purple) and High Camp (Blue) during the 2017 melt season. (d) same as in c but shown as lag from peak melting.

3.5 hours (Figures S7–S8). Over the same time period air temperature peaked two hours later, around 15:30±3.3 hours (Figure S7). Moreover, peak melting occurred consistently around 13:30 at both Low Camp and High Camp over the 2017 and 2018 melt seasons. Due to the similarity in observations between weather stations, we use a single timeseries of peak melting to quantify lags across all variables.

3.2 Meltwater delivery to moulins

Of the physical characteristics considered, catchment area exerted the strongest control on the timing of peak meltwater delivery to moulins. At Low Camp's main catchment JEME (0.2 km^2), meltwater delivery peaked around 15:30 (Figure 2b–c), lagging peak melt by 2.4 ± 1.6 hours over the period of 2 July–9 August 2017 (Figure 2d; Table S3). At High Camp's much larger RADI catchment (16.8 km^2), meltwater delivery peaked around 19:45, lagging peak melt by 6.5 ± 1.8 hours (Figure 2 and S11) over the period of 5–16 August 2017. The longer residence time of meltwater within the supraglacial drainage system at the larger, higher-elevation RADI catchment ultimately caused moulin input to peak four hours later in the day at RADI when compared to the smaller and lower-elevation JEME catchment (Figure 2b–c). Importantly, all of the underlying data used to generate the aforementioned timing of peak meltwater delivery for JEME and RADI catchments were collected during bare-ice conditions (see Figures S1 and S2 for photos of surface conditions). Bare-ice conditions therefore eliminate the influence of the seasonal snowpack on the timing of peak meltwater to moulins reported here.

Observations from our two auxiliary catchments confirm the pattern of longer lags between peak melting and peak meltwater delivery to moulins with increased catchment area (Figure 2a; Table S1). At Low Camp's JNIH (1.1 km^2; 13–20 July 2017) peak meltwater delivery lagged peak melting by 4.2 ± 1.8 hours, and by 5.0 ± 1.3 hours at High Camp's SBPI (2.4 km^2; August 2018). Altogether, observations from four catchments indicate there are increasing delays in the timing of meltwater delivery to larger, higher-elevation catchments (Figure 2a) within this sector of the western GrIS.

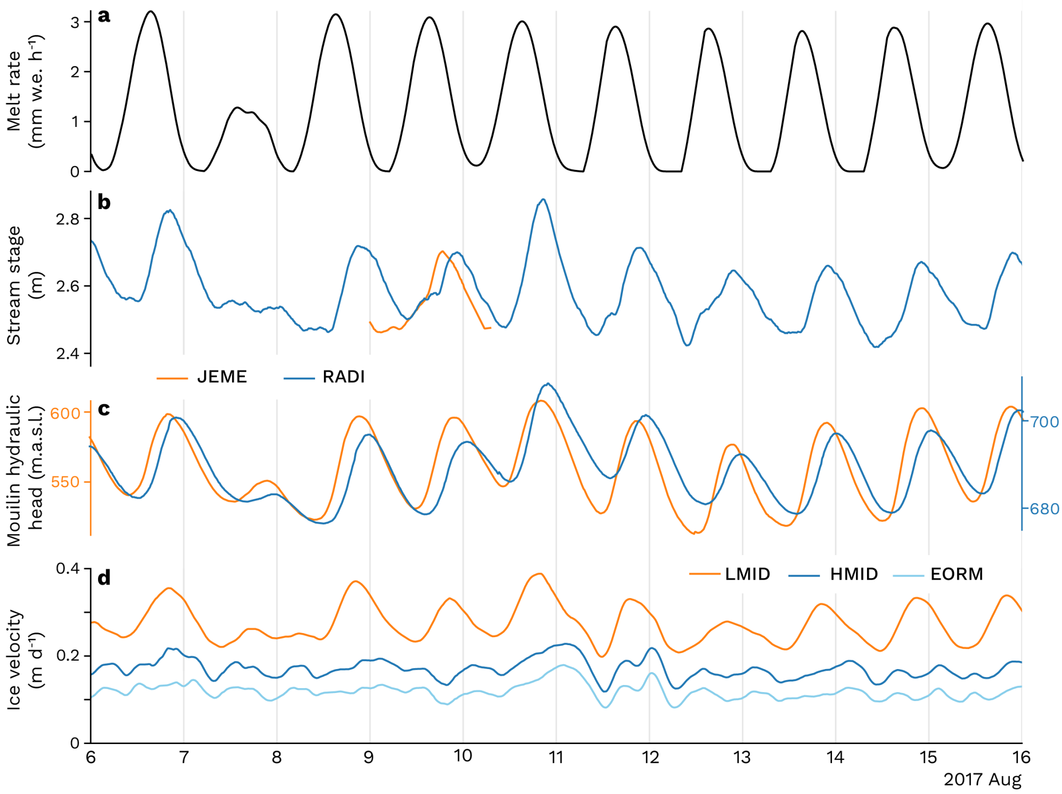

Figure 3. Comparison between Low Camp measurements (orange) and High Camp measurements (blue). (a) Meltwater production (b) supraglacial stream stage about an arbitrary datum. (c) Moulin hydraulic head from JEME moulin (left axis, orange) and RADI moulin (right axis, blue). The two axes are shown to highlight the phase-shift between the two timeseries (see Figure S12 for a single axes). (d) Along-flow ice velocity. Extended timeseries are shown in Figures S9 and S11.

3.3 Moulin hydraulic head and sliding

Coincident timeseries of moulin head from August 2017 (Figures 3, S9c–S11c) constrain the timing of peak pressures within the subglacial drainage system for Low Camp and High Camp moulins. The lag between peak meltwater delivery to moulins and peak moulin head was similar, approximately two hours, at both sites (Figures 2c–d and S15). However, the longer delay in meltwater delivery caused High Camp's RADI moulin's water level to peak 1–3.25 hours later in the day than at the lower-elevation JEME moulin (Figure S15). This delay resulted in a clear phase shift between the moulin head timeseries from JEME and RADI moulins (Figure 3c).

We find a strong agreement between the timing of peak moulin head and peak sliding speed at Low Camp that is not observed at High Camp. For example, peak sliding speed at Low Camp coincided with peak moulin head but lagged peak melting by 4.6 ± 1.7 hours (Figure 2d). This pattern was observed during 2017 and 2018 with peak sliding lagging peak moulin head by -0.4 ± 1.5 hours ($n = 21$) for JEME and -0.3 ± 2.3 hours ($n = 28$) for PIRA (i.e., sliding precedes head). In contrast, at High Camp peak sliding lagged (i.e. followed) peak moulin head by 2.8 ± 2.0 and 3.0 ± 1.2 hours for GNSS stations EORM and HMID respectively. Ultimately sliding peaked 2.2–7.6 hours later at High Camp than at Low Camp throughout the 2017 melt season (Figure 3d).

3.4 Glacio-hydraulic tremor amplitude

To investigate how transient surface conditions (i.e., seasonal snowpack removal and supraglacial drainage network evolution) within Low Camp's JEME catchment influence the timing of meltwater delivery to moulins, we utilize observations of glacio-hydraulic tremor amplitude to supplement stream stage observations which only cover 11 July and 20 August 2018 during bare-ice conditions (Figure 4 and S10). Our tremor amplitude timeseries spanned the entire duration of the melt season, from 5 June through the end of August 2018 ($n = 62$ for diurnal extrema picks). Peak meltwater delivery to PIRA moulin coincided with peak tremor amplitude (Figure S13; Text S4 and S7), which occurs when subglacial pressure gradients within moulin-connected subglacial channels are increasing most rapidly (Gimbert et al., 2016). From the monthly breakdown of diurnal extrema peaks shown in Figure 4, tremor amplitude peaked earlier in the day as the melt season progressed, lagging peak melting by 6.1 ± 2.2, 3.5 ± 2.5, and 1.4 ± 2.5 hours in June, July, and August respectively. Stream stage observations agree, with the lag between peak melting and peak meltwater delivery decreasing by 54 minutes between July and August 2018.

4 Discussion

4.1 Controls on the timing of peak moulin head

By constraining the timing of peak meltwater delivery to moulins within five GrIS catchments, we show that differences in the physical characteristics of catchments—area, snowpack extent, and supraglacial drainage efficiency—induce non-trivial heterogeneity in the timing of meltwater delivery to moulins. Lags between peak melting and peak meltwater delivery to moulins increased with catchment area (Figure 2a), resulting in longer delays in the timing of meltwater delivery to larger, higher-elevation catchments. This is expected because meltwater must be transported greater distances over the ice surface before reaching the catchment's terminal moulin (Sherman, 1932). Previous works have shown a positive relationship between catchment area and delays in meltwater delivery through applying traditional hydrological theory to supraglacial catchment throughout the GrIS ablation area (King, 2018; Smith et al., 2017; Yang & Smith, 2016; Yang et al., 2018). In considering 799 catchments in SW Greenland, Smith et al. (2017) showed that catchments with areas 0.4–244.9 km^2 could produce lags between peak melting and meltwater delivery to moulins of 0.4–9.5 hours. Our observations show that even a more limited range of catchment sizes (0.2–16.8 km^2) can induce differences of over four hours in the timing of meltwater delivery to moulins, thereby inducing a similar offset in timing of peak moulin head across the ablation area.

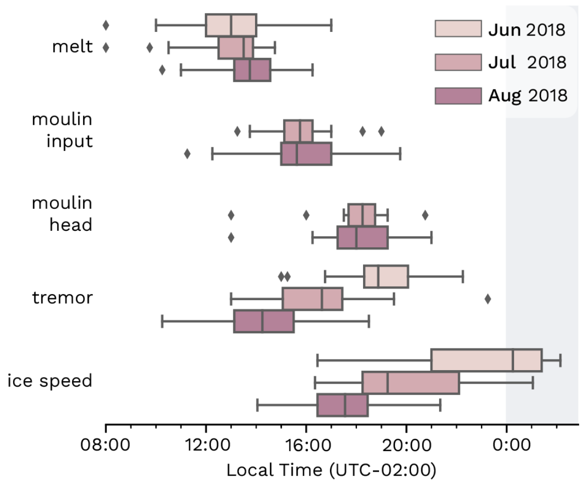

Figure 4. Seasonal shifts in meltwater propagation timing. Box and whisker plots show the monthly distribution of daily peaks in melting, meltwater input to PIRA moulin (stream stage), PIRA moulin head, tremor amplitude, and ice speed of Low Camp's JEME catchment during the 2018 melt season. Shading corresponding to the month of the underlying data for June (lightest), July (mid-tone), and August (darkest). Gray diamonds mark outliers, and the center line corresponds to median values. Shading as in Figure 2.

The timing of meltwater delivery to moulins within individual catchments evolves over the course of the melt season as the seasonal snowpack melts and then as efficient supraglacial stream networks form (Lampkin & Vanderberg, 2014; Willis et al., 2002; Yang et al., 2018). Early in the 2018 melt season (i.e., the first few weeks following the melt season's initiation on 6 June), snow cover was likely responsible for the increase in meltwater's residence time within the supraglacial drainage system as indicated by the difference in peak tremor amplitude and sliding velocity between June and July (Figure 4). This increased residence time would have delayed meltwater delivery to the Low Camp moulin PIRA during the first few weeks of the 2018 melt season as the snowline quickly retreated upglacier (Text S9). This approximately three hour increase is similar to previous work on Haut Glacier d'Arolla's La Vierge catchment (0.11 km^2) where Willis et al. (2002) showed the seasonal snowpack could increase the lag between peak melting and peak meltwater delivery by more than two hours. Despite being snow-free by July 2018, peak meltwater delivery to PIRA moulin decreased by 1–1.75 hours between July and August. This shorter residence time of meltwater within the supraglacial drainage system is likely attributed to increased supraglacial drainage density where small tributaries drain into well-developed streams and rivers which quickly transport meltwater to the catchment's terminal moulin (e.g., Yang & Smith, 2016).

By including direct measurements of moulin head within the primary catchments considered in this study, we identified a two hour lag between peak meltwater delivery and moulin head. The lag between peak meltwater delivery and moulin head was consistent throughout the melt season and between sites despite significant differences in the magnitude and timing of peak meltwater delivery to the moulins themselves (Figure 2c–d). This contrasts previous assumptions that peak meltwater delivery and moulin head would occurr simultaneously (e.g., McGrath et al., 2011). While our observations cannot be extrapolated to every moulin on the GrIS, they do demonstrate that there is a delay inherent to the coupled englacial-subglacial drainage system that controls the absolute timing of peak moulin head and therefore the timing of peak pressurization within moulin-connected parts of the subglacial drainage system.

4.2 Local relationships between effective pressure and ice motion

Lags between peak melting and peak sliding speed increased with distance from the ice sheet margin, echoing the pattern established by Hoffman et al. (2011). At Low Camp, peak moulin head and peak sliding speed were nearly coincident, indicating daily peaks in moulin head control the timing of peak subglacial water pressure and sliding. At High Camp, longer delays in meltwater delivery caused moulin head to peak 1–3.25 hours later than at Low Camp (Figure 3). However, this delay does not entirely account for the later timing of peak sliding, which lagged peak moulin head by up to 3.5 hours. Accordingly, the timing of peak moulin head was only partially responsible for the later timing of peak sliding. Instead the timing offset between peak pressure within the moulin-connected drainage system and peak sliding speed indicates there is a difference in the relationship between effective pressure (ice overburden pressure minus subglacial water pressure) and sliding at higher elevations that was not observed lower on the ice sheet.

The spatial distribution and density of moulins control the development of the subglacial drainage system by determining where meltwater is delivered to the bed and thus where subglacial conduits form (Banwell et al., 2016; Gulley et al., 2012). When moulin head is high, subglacial conduits become pressurized relative to the surrounding distributed drainage system, driving water out laterally away from the conduits and into neighboring linked-cavities (Bartholomaus et al., 2007; Hubbard et al., 1995; Rada & Schoof, 2018; Werder et al., 2013). As higher pressures migrate out into the distributed system, basal traction is reduced over a larger area of the bed, thereby promoting sliding. Because sliding is controlled by the areally integrated basal traction over three to eight ice thicknesses (Gudmundsson, 2003), peak sliding should occur when high pressures cover the largest area of the bed. At lower elevations on the ice sheet where moulin density is high (e.g., Low Camp's primary catchment with more than 10 moulins per km^2; Figure S4), closely spaced subglacial conduits work in tandem to quickly pressurize a large area of the bed. However, at higher elevations where moulin density is much lower (e.g., High Camp with 1–3 moulins per km^2; Figure S5), sliding will be more coupled to the pressure change emanating from an individual conduit as it migrates into the distributed system. Modeling work by Werder et al. (2013) showed that the diurnal pressurization of a single conduit can extend up to two kilometers into the distributed system, with the water pressure perturbation amplitude decreasing with distance away from the conduit, while also incurring a progressive phase lag of up to six hours. In this paradigm, the finite diffusion speed of the pressure change within the conduit at the base of RADI moulin could produce the two hour lag between peak moulin head and peak sliding observed at our higher-elevation site.

4.3 Implications

Our results reinforce previous observations of spatially inhomogeneous patterns of GrIS ice motion driven by areas with direct hydraulic connections to the bed, while highlighting the added complexity induced by the differences in timing of peak moulin head throughout the ablation area. Longitudinal flow coupling acts over a range of length-scales, explaining acceleration in areas of the GrIS without direct hydraulic connections to the bed (Price et al., 2008; Ryser et al., 2014). Areas without direct hydraulic connections (i.e., without moulins), respond passively to ice motion induced by pressure fluctuations within moulin-connected parts of the subglacial drainage system (Ryser et al., 2014). At our lower elevation site, moulin head and sliding speeds peaked consistently earlier than at higher elevations. Accordingly, when peak pressurization (or "slipperiness") was reached at lower elevations, upglacier areas were still resisting flow, and vice versa. This observed offset in the timing of peak pressurization may then produce different patterns of ice deformation, stress transfer, and basal motion, than would be expected if all areas with moulins experienced peak pressurization coincidentally.

Alpine glaciers have been frequently used as analogues to the GrIS, yet their usefulness remains a point of debate. Fundamental relationships between hydrology and ice motion identified within alpine environments diverge with distance inland as the ice thickens, surface slopes flatten, and moulin density decreases. Our results demonstrate the correlation between moulin head and peak sliding initially identified on alpine glaciers (Iken, 1972) seems to hold in areas with high moulin density (e.g., Low Camp). This relationship likely remains intact in this area because closely-spaced moulins are able to feed water simultaneously to the entirety of the ice sheet bed (Andrews et al., 2014). However, at higher elevations where moulin density is low (e.g., High Camp), the same correlation between moulin head and peak sliding is not observed. Accordingly, the straightforward coupling between effective pressure and ice motion derived from studies on alpine glaciers breaks down for inland reaches of the GrIS ablation area. Resolving the distinct processes governing hydrodynamic coupling within these areas will be more important as the GrIS ablation area continues to expand further inland as the climate warms (Noël et al., 2019).

5 Conclusions

Our observations suggest the supraglacial drainage system controls hydrodynamic coupling by two mechanisms: by creating delays in meltwater routing that propagate through the englacial and subglacial drainage systems and by controlling the spatial distribution of moulins which affects relationships between effective pressure and sliding. Because moulin density and catchment area are inherently linked, these processes work together to produce the progressively later timing daily peak sliding speeds with increasing distance from the ice sheet's margin. Given the role of the supraglacial drainage system in controlling the timing of peak subglacial pressurization, we would expect the well-documented heterogeneity of supraglacial catchments (King, 2018; Smith et al., 2017; Yang & Smith, 2016) to produce widespread variability in the timing of peak pressurization experienced within different regions of the subglacial drainage system. How these complex patterns of subglacial pressurization influence ice flow need to be considered in order to determine how the GrIS will respond to increased melting under future climatic warming.

Acknowledgments

This work was supported by the United States National Science Foundation grant number 1604022. GNSS station support was provided by UNAVCO in collaboration with the National Science Foundation. Thank you to Victoria Siegel and Ronald Knoll for assistance in the field. Polar Field Services, Inc. provided logistical support, and special thanks to Kathy Young for her work supporting field campaigns. ArcticDEM provided by the Polar Geospatial Center under NSF-OPP awards 1043681, 1559691, and 1542736. DEM(s) were created from DigitalGlobe, Inc., imagery and funded under National Science Foundation awards 1043681, 1559691, and 1542736.

Data Availability Statement

The data sets and code used in this study are openly available. Meteorological and hydrological data sets are archived with the National Science Foundation's Arctic Data Center through the MoVE project's portal: `http://arcticdata.io/catalog/portals/moulin` (Mejia, Trunz, Covington, & Gulley, 2020; Mejia, Trunz, Covington, Gulley, & Breithaupt, 2020; Mejia et al., 2021). GC-Net weather station data from JAR1 is available from (Steffen et al., 1996) and is also archived with (Mejia et al., 2021) for convenience. Data from our on-ice GNSS stations and the base stations used during processing are archived through UNAVCO's GAGE Facility (Fahnestock et al., 2006; Mejia, Gulley, & Dixon, 2020). The Python module created to pick diurnal extrema is archived with Zenodo (see Mejia, 2022).

References

Andrews, L. C., Catania, G. A., Hoffman, M. J., Gulley, J. D., Lüthi, M. P., Ryser, C., . . . Neumann, T. A. (2014). Direct observations of evolving subglacial drainage beneath the Greenland Ice Sheet. *Nature*, *514*(7520), 80–83. doi: 10.1038/nature13796

Banwell, A. F., Hewitt, I. J., Willis, I. C., & Arnold, N. S. (2016). Moulin density controls drainage development beneath the Greenland ice sheet. *Journal of Geophysical Research: Earth Surface*, *121*(12), 2248–2269. doi: 10.1002/2015JF003801

Bartholomaus, T. C., Anderson, R. S., & Anderson, S. P. (2007). Response of glacier basal motion to transient water storage. *Nature Geoscience*, *1*, 33–37. doi: 10.1038/ngeo.2007.52

Bartholomaus, T. C., Larsen, C. F., Amundson, J. M., O'Neel, S., Walter, J. I., & West, M. E. (2015). Subglacial discharge at tidewater glaciers revealed by seismic tremor. *Geophysical Research Letters*, *42*, 6391–6398. doi: 10.1002/2015GL064590

Clason, C. C., Mair, D. W., Nienow, P. W., Bartholomew, I., Sole, A. J., Palmer, S., & Schwanghart, W. (2015). Modelling the transfer of supraglacial meltwater to the bed of Leverett Glacier, Southwest Greenland. *Cryosphere*, *9*(1), 123–138. doi: 10.5194/tc-9-123-2015

Fahnestock, M. A., Truffer, M., SDFE, T. D. A., & Community, U. (2006). *Greenland GNSS Network - KAGA-Kangia North P.S.,.* UNAVCO. doi: 10.7283/FQGY-4535

Gimbert, F., Tsai, V. C., Bartholomaus, T. C., Amundson, J. M., & Walter, J. I. (2016). Subseasonal changes observed in subglacial channel pressure, size, and sediment transport. *Geophysical Research Letters*, *43*(September), 3786–3794. doi: 10.1002/2016GL068337

Goelzer, H., Nowicki, S., Payne, A., Larour, E., Seroussi, H., Lipscomb, W. H., . . . Van Den Broeke, M. (2020). The future sea-level contribution of the Greenland ice sheet: A multi-model ensemble study of ISMIP6. *Cryosphere*, *14*, 3071–3096. doi: 10.5194/tc-14-3071-2020

Gudmundsson, G. H. (2003). Transmission of basal variability to a glacier surface. *Journal of Geophysical Research: Solid Earth*, *108*(B5), 1–19. doi: 10.1029/2002jb002107

Gulley, J. D., Grabiec, M., Martin, J. B., Jania, J., Catania, G. A., & Glowacki, P. S. (2012). The effect of discrete recharge by moulins and heterogeneity in flow-path efficiency at glacier beds on subglacial hydrology. *Journal of Glaciology*, *58*(211), 926–940. doi: 10.3189/2012JoG11J189

Hoffman, M. J., Catania, G. A., Neumann, T. A., Andrews, L. C., & Rumrill, J. A. (2011). Links between acceleration, melting, and supraglacial lake drainage of the western Greenland Ice Sheet. *Journal of Geophysical Research: Earth Surface*, *116*(4), 1–16. doi: 10.1029/2010JF001934

Hubbard, B., Sharp, M. J., Willis, I. C., Nielsen, M. K., & Smart, C. (1995). Borehole water-level variation and the structure of the subglacial hydrological system of Haut Glacier d'Arolla, Valais, Switzerland. *Journal of Glaciology*, *41*(139), 572–583.

Iken, A. (1972). Measurements of Water Pressure In Moulins as Part of A Movement Study of the White Glacier, Axel Heiberg Island, Northwest Territories, Canada. *Journal of Glaciology*, *11*(61), 53–58.

King, L. A. (2018). *Identifying and characterizing the spatial variability of supraglacial hydrological features on the western Greenland Ice Sheet* (Doctoral dissertation, University of British Columbia). doi: 10.14288/1.0372827

Lampkin, D. J., & Vanderberg, J. (2014). Supraglacial melt channel networks in the Jakobshavn Isbræ region during the 2007 melt season. *Hydrological Processes*, *28*(25), 6038–6053. doi: 10.1002/hyp.10085

McGrath, D., Colgan, W. T., Steffen, C., Lauffenburger, P., & Balog, J. (2011). Assessing the summer water budget of a moulin basin in the sermeq avannarleq ablation region, Greenland ice sheet. *Journal of Glaciology*, *57*(205), 954–964. doi: 10.3189/002214311798043735

Mejia, J. Z. (2022, July). *jzmejia/diurnalextrema: v1.0.0.* Zenodo. Retrieved from `https://doi.org/10.5281/zenodo.6812156` doi: 10.5281/zenodo.6812156

Mejia, J. Z., Gulley, J. D., & Dixon, T. H. (2020). *West Greenland Moulins 2017-2019 Sermeq Avannarleq - GPS/GNSS Observations Dataset.* The GAGE Facility operated by UNAVCO, Inc. doi: 10.7283/VT31-EK40

Mejia, J. Z., Gulley, J. D., Trunz, C., Covington, M. D., Bartholomaus, T. C., Xie, S., & Dixon, T. (2021). Isolated cavities dominate Greenland Ice Sheet dynamic response to lake drainage. *Geophysical Research Letters*, 1–11. doi: 10.1029/2021gl094762

Mejia, J. Z., Trunz, C., Covington, M. D., & Gulley, J. D. (2020). *Meteorological data from two on-ice weather stations at 780 and 950 m asl elevations in the ablation area of Sermeq Avannarleq, West Greenland from 2017-2018.* Arctic Data Center. doi: 10.18739/A2CF9J745

Mejia, J. Z., Trunz, C., Covington, M. D., Gulley, J. D., & Breithaupt, C. (2020). *Moulin hydrological measurements from Sermeq Avannarleq, West Greenland Ice Sheet from 2017-2018.* Arctic Data Center. doi: 10.18739/A2M03XZ13

Morlighem, M., Williams, C. N., Rignot, E., An, L., Arndt, J. E., Bamber, J. L., … Zinglersen, K. B. (2017). BedMachine v3: Complete Bed Topography and Ocean Bathymetry Mapping of Greenland From Multibeam Echo Sounding Combined With Mass Conservation. *Geophysical Research Letters*, *44*(21), 11,051–11,061. doi: 10.1002/2017GL074954

Noël, B., van de Berg, W. J., Lhermitte, S., & van den Broeke, M. R. (2019). Rapid ablation zone expansion amplifies north Greenland mass loss. *Science Advances*, *5*(9), 2–11. doi: 10.1126/sciadv.aaw0123

Pellicciotti, F., Brock, B., Strasser, U., Burlando, P., Funk, M., & Corripio, J. (2005). An enhanced temperature - index glacier melt model including the shortwave radiation balance : development and testing for Haut Glacier d ' Arolla , Switzerland. *Journal of Glaciology*, *51*(175), 573 – 587. doi: 10.3189/172756505781829124

Price, S. F., Payne, A. J., Catania, G. A., & Neumann, T. A. (2008). Seasonal acceleration of inland ice via longitudinal coupling to marginal ice. *Journal of Glaciology*, *54*(185), 213–219. doi: 10.3189/002214308784886117

Rada, C., & Schoof, C. (2018). Channelized, distributed, and disconnected: subglacial drainage under a valley glacier in the Yukon. *The Cryosphere*, *12*(8), 2609–2636. Retrieved from `https://doi.org/10.5194/tc-12-2609-2018` doi: 10.5194/tc-12-2609-2018

Rennermalm, Å. K., Moustafa, S. E., Mioduszewski, J., Chu, V. W., Forster, R. R., Hagedorn, B., … Tedesco, M. (2013). Understanding Greenland ice sheet hydrology using an integrated multi-scale approach. *Environmental Research Letters*, *8*(1). doi: 10.1088/1748-9326/8/1/015017

Ryser, C., Lüthi, M. P., Andrews, L. C., Catania, G. A., Funk, M., & Hawley, R. L. (2014). Caterpillar-like ice motion in the ablation zone of the Greenland ice sheet. *Journal of Geophysical Research : Earth Surface*, *119*, 2258–2271. doi: 10.1002/2013JF003067.Received

Sherman, L. K. (1932). The Relation of Hydrographs of Runoff to Size and Character of Drainage-Basins. *Eos, Transactions American Geophysical Union*, *13*(1), 332–229.

Smith, L. C., Chu, V. W., Yang, K., Gleason, C. J., Pitcher, L. H., Rennermalm, Å. K., … England, J. H. (2015). Efficient meltwater drainage through supraglacial streams and rivers on the southwest Greenland ice sheet. *Proceedings of the National Academy of Sciences*, *112*(4), 1001–1006. doi:

10.1073/pnas.1413024112

Smith, L. C., Yang, K., Pitcher, L. H., Overstreet, B. T., Chu, V. W., & Rennermalm, Å. K. (2017). Direct measurements of meltwater runoff on the Greenland ice sheet surface. *Proceedings of the National Academy of Sciences*, *114*(50), 1–10. doi: 10.1073/pnas.1707743114

Steffen, C., Box, J. E., & Abdalati, W. (1996). Greenland Climate Network: GC-Net. *Cold Regions Research and Engineering Laboratory*, *CRREL Spec*, 98–103.

Werder, M. A., Hewitt, I. J., Schoof, C., & Flowers, G. E. (2013). Modeling channelized and distributed subglacial drainage in two dimensions. *Journal of Geophysical Research: Earth Surface*, *118*(4), 2140–2158. doi: 10.1002/jgrf.20146

Willis, I. C., Arnold, N. S., & Brock, B. W. (2002). Effect of snowpack removal on energy balance, melt and runoff in a small supraglacial catchment. *Hydrological Processes*, *16*(14), 2721–2749. doi: 10.1002/hyp.1067

Yang, K., & Smith, L. C. (2016). Internally drained catchments dominate supraglacial hydrology of the southwest Greenland Ice Sheet. *Journal of Geophysical Research : Earth Surface*, *121*, 1891–1910. doi: 10.1002/2016JF003927

Yang, K., Smith, L. C., Karlstrom, L., Cooper, M. G., Tedesco, M., & van As, D. (2018). A new surface meltwater routing model for use on the Greenland Ice Sheet surface. *The Cryosphere*, *12*, 3791–3811. doi: 10.5194/tc-12-3791-2018

Supporting Information for "Moulin density controls the timing of peak pressurization within the Greenland Ice Sheet's subglacial drainage system"

J. Z. Mejia[1], J. D. Gulley[2], C. Trunz[3], M. D. Covington[4], T. C. Bartholomaus[5], C. Breithaupt[6], S. Xie[7], T. H. Dixon[2]

[1]Department of Geology, University at Buffalo, Buffalo, NY 14260

[2]Department of Geosciences, University of South Florida, Tampa, FL 33620.

[3]Department of Applied Geomatics, Université de Sherbrooke, Sherbrooke, QC J1K 2R1, Canada

[4]Department of Geosciences, University of Arkansas, Fayetteville, AR 72701

[5]Department of Earth and Spatial Sciences, University of Idaho, Moscow, ID 83844

[6]Exxonmobil Upstream Research Company, Spring, TX 77389

[7]Department of Civil and Environmental Engineering, University of Houston, Houston, TX 77204

Supplement Contents

Introduction

This supplement provides additional information relating to the main text and details on methodology. **Text S1** describes the characteristics of the catchments studied at Low Camp and High Camp. **Text S2** describes the methodology used to delineate catchment boundaries and calculate each catchment's area. **Text S3** details our meteorological measurements and the model used to calculate meltwater production. **Text S4** details our measurements of supraglacial stream stage and discusses stream discharge measurements that we report in **Table S3**. In **Text S5** we provide more details on moulin instrumentation. **Text S6** explains the methodology used in post-processing GNSS station data and calculating surface ice velocity. **Text S7** details the analysis of seismic data to resolve glaciohydraulic tremor amplitude. **Text S8** discusses how we identified diurnal extrema values across our timeseries data sets using the `DiurnalExtrema` python module developed for this study. Finally, **Text S9** elaborates on how diurnal extrema timing changes over the course of the 2018 melt season at our lower elevation site.

Text S1. Catchment characteristics

We instrumented a total of three moulins during this study. At Low Camp, we instrumented moulins draining the same catchment (0.2 km^2 area) in both the 2017 and 2018 melt seasons. We instrumented moulin JEME on 20 July 2017 and moulin PIRA on 10 July 2018. PIRA moulin formed by a crevasse cross-cutting the supraglacial stream feeding JEME moulin after it was advected approximately 90 m downglacier (Figure S3). By instrumenting PIRA moulin, we measured water pressures in the same region of the subglacial drainage system in both years. Low Camp has a high moulin density with at least eight other moulins within a 1 km radius of moulin JEME and PIRA in 2017 and 2018 (Figure S4). Additionally, there are two crevasse fields within 2 km of our instrumented moulins, one to the east and the other to the southwest. We instrumented Radical (RADI) moulin at High Camp during the 2017 melt season. Radical moulin drained a catchment with an area of ~ 16.6 km^2. High Camp had a much lower moulin density with one moulin within a 1 km radius of RADI moulin with a single crevasse located approximately 250 m downglacier (Figure S5).

Text S2. Catchment delineation

To delineate internally drained catchments, we corrected automatically determined boundaries by visual inspection of remote sensing imagery. We use ArcticDEM mosaic with a ground sample distance of two meters (Porter et al., 2018) derived from the panchromatic bands of WorldView satellites in the DigitalGlobe optical imaging constellation. We project the DEMs into the WGS84 / NSIDC Sea Ice Polar Stereographic North coordinate reference system (EPSG:3413). This Polar Stereographic projection is based on the World Geodetic System 1984 ellipsoid (WGS84). We performed the following steps to delineate supraglacial catchments from the DEM mosaic: First, we applied an algorithm to identify and fill topographic sinks (Conrad et al., 2015; Wang & Liu, 2006) while preserving the downward slope of the flow path (i.e., the minimum slope gradient between cells). Then we used the created depressionless DEM to calculate supraglacial flow accumulation via the steepest descent algorithm (flow into and out of each grid element). This methodology produces a shapefile of predicted supraglacial stream locations. By prescribing moulin locations we are then able to define supraglacial catchment boundaries. We then manually inspect these predicted catchment boundaries by comparing them to high-resolution WorldView imagery. Where mismatches between catchment boundaries and actual supraglacial flow paths are

0094-8276/22/$5.00

identified, we adjust the catchment polygon to reflect the actual stream routing locations.

Text S3. Meteorological measurements

To quantify the timing and magnitude of surface melting we installed automatic weather stations at our lower and higher elevation field sites. The LOWC weather station was installed at Low Camp (69.4727°N, 49.8263°W, 780 m.a.s.l.) on 2 July and the HIGH weather station was installed at High Camp (69.5416°N, 49.7100°W, 950 m.a.s.l.) on 28 July 2017 (Mejia, Trunz, Covington, & Gulley, 2020). Each weather station was equipped with a Onset ®HOBO ®U30-NRC data logger mounted onto aluminum conduit frozen into the ice that recorded meteorologic measurements every 15 minutes. The 10 Ahr battery powering each logger was recharged by a 5 W solar panel. Peripheral sensors were mounted above the data logger so that they were ~ 2 m above the ice surface at the time of instillation. Air temperature was measured using an air temperature and relative humidity smart sensor installed within a solar radiation shield. We measured incoming and reflected shortwave solar radiation using two silicon pyranometers mounted onto a bracket that extended the sensors 42 cm from the station's mast. Incoming radiation was measured by our upward pointing sensor and reflected radiation was measured by our downward pointing sensor.

The HOBO/Onset weather stations deployed at our (LOWC) Low Camp and (HIGH) High Camp field sites recorded air temperature, incoming and outgoing solar radiation, along with other measurements, at 15 minute intervals. We use meteorological measurements from the GC-NET weather station JAR1 to fill in data gaps. We calculate melt rate M with units of (mm w.e. h^{-1}) from air temperature T and incoming shortwave radiation G measurements for each weather station using an enhanced temperature-index melt model (Pellicciotti et al., 2005):

$$M = \begin{cases} TF\mathrm{T} + SRF(1-\alpha)\mathrm{G} & \text{if T} > \mathrm{T}_T \\ 0 & \text{if T} \geq \mathrm{T}_T \end{cases} \tag{1}$$

where TF is a temperature factor (TF=0.05 mm h^{-1} °C^{-1}), SRF is a shortwave radiation factor (SRF=0.0094 m^2 mm W^{-1} h^{-1}), α is daily ice surface albedo, and T_T is a threshold temperature taken to be 0°C under which no melting occurs (Mejia, Trunz, Covington, & Gulley, 2020).

Incoming shortwave radiation measurements were corrected for errors resulting from shadows cast on the weather station. The drop in solar radiation caused by the shadow is systematic, occurring between 11:00–13:00 UTC though the melt season. We applied a multidimensional median filter to the incoming solar radiation timeseries to account for these errors. Daily albedo values were determined using incoming and reflected solar radiation measurements from 15:00 UTC, when incoming solar radiation is at its peak and the solar zenith angle (θ) is less than 50° (Pellicciotti et al., 2005). In 2018, only one solar radiation sensor was functional upon return to our LOWC weather station, we used that sensor to record incoming solar radiation. As such, we were unable to calculate daily albedo values and instead use a constant value of 0.7 for all 2018 melt rate calculations. The timing of peak daily melt is unaffected by this choice of albedo.

Ice surface ablation was monitored by our stream gauging stations (Figure S1c) during the 2017 and 2018 melt seasons using a Global Water Ultrasonic distance sensor WL705-012. The sensors were affixed to aluminum conduit frozen into the ice surface via a steel extension arm. This sensor was powered and controlled by the stream gauging station's Campbell Scientific CR1000 data logger which recorded measurements every 15-minutes. We compare melt rate calculated using Equation 1 to our observations of ice surface lowering and find good agreement in magnitude (Figure S6) and in timing (Figures S7 and S8) for coincident measurements between 13 July through 19 August 2017. Figure S6 shows the observed surface lowering measurements converted to water equivalent using various ice densities. We find that using an average ice density of 0.7 g cm^{-3} produces the best fit to calculated melt rates. Hourly ice surface ablation is compared to calculated melt rate and air temperatures in Figure S7 and the diurnal extrema picks are shown in Figure S8. Calculated peak melting occurred on average at 13:30±1.0 hours (n = 37), agreeing with ablation measurements which show an average peak at 13:30±3.4 hours (n = 20). We also find that air temperature peaks two hours later than melting, occurring at 15:30±3.3 hours (n = 35).

Text S4. Supraglacial stream stage and discharge measurements

We monitor the timing of meltwater delivery to moulins by measuring the water level (or stream stage) of supraglacial streams just upstream their terminal moulins. We installed gauging stations ~ 30 m upstream of each stream's terminal moulin. Each gauging station was equipped with a Global Water ultrasonic water level sensor (model WL705-048 or WL705-012) affixed to a self-lowering crossbar mounted on either side of the supraglacial stream (Figures S1–S2). Campbell Scientific CR1000 data loggers equipped with DCDC-18R voltage boost regulators supplied power to the ultrasonic water level sensors. Data loggers were programmed to power on the water level sensor every 15 minutes and record the distance to the water's surface following a 15 second stabilization period. This 15 second averaging window reduces the influence of turbulence on the water level measurement. We use 100 Ω current shunt modules to convert the current output by the ultrasonic water level sensor into a voltage that can be measured by the data logger. We determine stream stage using an arbitrary datum of four meters below the face of each ultrasonic water level sensor. We use these measured water level fluctuations to constrain the timing of peak meltwater delivery to moulins (i.e., peak daily stream water level).

We measured the stage for the supraglacial streams draining into instrumented moulins during 2017 and 2018 (Tables S1 and S2). In 2017 we measured stream stage within the supraglacial streams terminating into JEME moulin at Low Camp and RADI moulin at High Camp. During the 2018 melt season, we monitored stream stage within JEME catchment at Low Camp. To better constrain the influence of catchment area on the timing of meltwater delivery to moulins we measured stream stage at two auxiliary sites near each camp—a catchment named JNIH near Low Camp and SBPI near High Camp (Figure 1). The catchment JNIH has an area of 1.1 km^2, and SBPI catchment has an area of 2.4 km^2 (Table S3). The average timing of peak meltwater delivery to the moulins draining these auxiliary catchments is shown in Figure 2a.

Supraglacial stream discharge: We collected point measurements of supraglacial stream discharge using two methods: (1) constant rate tracer injection method and (2) by using a continuous wave Doppler. In 2017 we used dye injection exclusively whereas in 2018 we used a combination of the two methods which are explained in detail below. We use the point measurements of stream discharge to calibrate a simple unit hydrograph model so that we can compare all of the instrumented catchments without incorporating biases deriving from measurement length, melt intensity, or timing within the melt season.

During the 2017 melt season, we measured stream discharge using the constant rate tracer injection method (Kilpatrick & Cobb, 1985). A known concentration (200 or 40 ppb) of Rhodamine dye was injected at a rate of 2 ± 0.5 mL per minute using a peristatic pump into into each stream 50–100 upstream of a Turner Cyclops-7 submersible fluorometer that measured dye concentration every three seconds. The distance between the dye injection point and fluorometer exceeded 200 stream widths, allowing the dye to fully mix within the water column. Stream discharge (Q, $\mathrm{m}^3\mathrm{s}^{-1}$) can then be calculated using:

$$Q = q\left(\frac{C_1}{C_2}\right) \tag{2}$$

where q is the rate of tracer injection into the supraglacial stream, C_1 is the concentration of the Rhodamine dye injection solution (mg L^{-1}), and C_2 is the fluorometer measured dye concentration. We estimated the error of measurements to be ±25% due to small variations in pump rate (1.5–2.5 ml s^{-1}).

During the 2018 melt season we incorporated the use of a Teledyne ISCO 2150 Area Velocity Flow Module to measure supraglacial stream discharge. This instrument measures stream level and average stream velocity to calculate the volume and rate of flow within open-channel streams. The instrument's Area Velocity (AV) sensor is mounted on the base of the supraglacial stream. The AV sensor is equipped with a piezo-resistive transducer that measures the liquid level above the stream's base. Water level calculations consider current atmospheric pressure through an internal vent tube that connects to the AV module on the ice surface. The produced water level measurements have an accuracy of 0.003 m, and a typical long term stability of ±0.007 m yr^{-1} The AV sensor also measures flow velocity by using the Doppler effect and ultrasonic sound waves (error of ±0.03 m s^{-1} or ±2% of reading). The pair of ultrasonic transducers located within the sensor emit and receive sound waves. The emitted and received wave frequency is then compared to determine flow velocity because the degree of change is proportional to the stream's velocity. We use these measurements in conjunction with a measured profile of the supraglacial stream to calculate the volume of water flowing into the stream's terminal moulin. We used a U-shape for PIRA stream with one meter width, and a rectangular shape for SBPI stream with a 10.4 m width.

Point measurements of stream discharge were compared to yield the average values reported in (Table S3) by using the Synthetic Unit Hydrograph (SUH) (King, 2018; Smith et al., 2017). The SUH curve calculates moulin discharge q (hr^{-1}) at time t using:

$$q(t) = e^m\left[\frac{t}{t_p}\right]^m\left[e^{-m\left(\frac{t}{t_p}\right)}\right]h_p \tag{3}$$

where m is the equation shape factor, t_p is time to peak discharge in hour (our measured lag time between peak melting and peak stream discharge), and h_p is peak discharge (hr^{-1}). We estimate hourly moulin hydrographs by convolving hourly melt data (M) with the SUH produced q-curve.

$$Q = M * q \tag{4}$$

here, $*$ is the convolution operator that we implement using NumPy's `convolve` function. The full SUH calculation is available in the Jupyter Notebook `calcSUH.ipynb` archived with Arctic Data (see Trunz et al., 2021).

Text S5. Moulin instrumentation

We instrumented a total of three moulins during the 2017 and 2018 melt seasons after the snowline retreated past each field site. At Low Camp, we instrumented moulin JEME on 20 July 2017 and moulin PIRA the following melt season on 10 July 2018. PIRA moulin formed by a crevasse crosscutting the supraglacial stream feeding JEME moulin after it was advected approximately 90 m downglacier (Figure S3). By instrumenting PIRA moulin, we measured water pressures in the same region of the subglacial drainage system in both years. At High Camp, we initially instrumented RADI moulin on 29 July 2017 (Mejia, Gulley, & Dixon, 2020). We used the same equipment and methodology to instrument all moulins in both years.

Moulin instrumentation was preformed using the following procedure. Geokon 4500-HD piezometers affixed to armored cable was lowered into moulins by measured lengths to constrain the distance from the ice-surface to the water column within each moulin. Campbell Scientific CR1000 data logger readings indicated that during the lowering process we encountered points where lowering additional cable did not increase the piezometer's reported submerged depth. We anchored the piezometers at the ice surface just above these elevations within the moulins, initially resulting in a truncated timeseries whenever water level fell below the sensor's submerged depth. In 2017 we were able to further lower the piezometer following the initial installation (on 23 July for JEME moulin and 6 August for RADI moulin) allowing us to record the full range of daily water level fluctuations within JEME and RADI moulins. After installation Campbell data loggers were programmed to record water level readings every 15 minutes.

Piezometric measurements of water pressure (P_w) were converted to hydraulic head (h) with the assumption of a vertical moulin shaft following:

$$h = \frac{P_w}{\rho_w g} + z_{sensor} \tag{5}$$

where ρ_w is the density of water, g is acceleration due to gravity, and z_{sensor} is the piezometer's elevation in meters above sea level. In 2017 we were able to correct our measurements of moulin hydraulic head for atmospheric pressure variability recorded at the GC-NET weather station JAR1. Due to instrument failure we were not able to correct our 2018 observations. Fortunately, the uncertainty added by the lack of atmospheric pressure correction is small (on the order of centimeters) compared to diurnal moulin water level variability (on the order of tens of meters). A comparison of corrected and uncorrected moulin hydraulic head timeseries for the 2017 melt season is shown in Figure S2 of Mejia et al. (2021).

Text S6. GNSS data processing

We use data acquired from four on-ice Global Navigation Satellite System (GNSS) stations to capture the ice-dynamic response to meltwater inputs to moulin-connected drainage systems at both of our field sites (Mejia, Trunz, Covington, Gulley, & Breithaupt, 2020). GNSS station JEME was co-located with moulin JEME in 2017 and moulin PIRA in 2018, and station RADI was co-located with RADI moulin in 2017. We use measurements from nearby stations to fill gaps in our timeseries. We used TRACK software, which utilizes carrier-phase differential processing relative to bedrock mounted base stations. We use base station KAGA with a ~ 28 km baseline length (Fahnestock et al., 2006)and station

ROCK with a ~ 36 km baseline length (Mejia, Trunz, Covington, Gulley, & Breithaupt, 2020) to determine kinematic site positions of our on-ice GNSS stations (Herring et al., 2010; Xie et al., 2019). We transform station positions to the along-flow direction and apply a centered 6 hour moving average filter to reduce noise while preserving diurnal variability, using this timeseries to calculate ice velocities. By centering this filter with respect to time, we maintain the timing of velocity extrema as has been previously demonstrated (e.g., ?, ?; Mejia et al., 2021).

Text S7. Seismic glaciohydraulic tremor

To further characterize water flow within the subglacial drainage system, we installed the seismic station SELC nearby JEME catchment before the melt season began in April 2018. The amplitude of glaciohydraulic tremor depends on the flux and pressure gradient of turbulent water flowing within well-connected subglacial conduits (Bartholomaus et al., 2015; Gimbert et al., 2016). Seismic station SELC was equipped with a Nanometrics Centaur digitizer and a Nanometrics Trillium compact posthole sensor that was covered in sand to improve sensor-ice coupling. The raw, recorded waveforms were corrected for their instrument responses. We determined glaciohydraulic tremor amplitude as the 20th percentile amplitude of 10 minute, enveloped, vertical, velocity seismic waveforms, high-pass filtered above 2 Hz (see Mejia et al., 2021, for more details). See Röösli et al. (2014) a more thorough discussion of the differences in seismic signals associated with other seismic sources—shallow and deep icequakes, and long duration (> 30 minute) tremor from moulin activity—that we do not consider in this study.

Text S8. Diurnal extrema picks

We determined diurnal extrema values from timeseries observations using the `DiurnalExtrema` python module created for this project. This module determines diurnally varying extrema by implementing specific specifications for local extrema picks. In addition to limiting the number of maximum and minimum extrema picks to one per day (24 hour period), requiring the minimum value precede the maximum, or allowing an extrema to fall outside of the 24 hour calendar day. This module is open-source and can be accessed through GitHub or Zortoro, see the data availability statement following the main text for details.

Figures S9–S11 show timeseries data sets with diurnal extrema picks used to generate the statistics described with the main text, underlying Figures 2 and 4, and reported by Table S3. Data collected at Low Camp during the 2017 melt season is plotted in Figure S9. Supraglacial stream stage shown for the auxiliary catchment JNIH (orange) and our main catchment JEME (blue) (Figure S9b). Because we are only interested in diurnal meltwater propagation, we exclude the spike in stream stage on 24 July 2017 that coincided with a period of heavy rainfall. Spikes in the moulin hydraulic head (Figure S9c) and ice velocity (Figure S9d) on 27 July 2017 were similarly excluded because they were caused by a subglacial floodwave following the rapid draining of upglacier supraglacial lakes rather than by diurnal meltwater inputs to JEME moulin. We recorded a similar event on 25 July 2018 and similarly exclude the dates from extrema picks (Figure S10), and exclude dates corresponding to recorded rainfall.

Text S9. Seasonal evolution

To determine how snowpack removal and increased supraglacial drainage efficiency influence the timing of meltwater delivery to moulins, we explore how lags in meltwater propagation changed throughout the 2018 melt season at Low Camp. Lags between peak melting and all other variables decreased as the melt season progressed (Figure 4), with the most considerable change occurring between June and July. On diurnal timescales, peak tremor amplitude occurs near the time of peak meltwater delivery to PIRA moulin (Figure S13), when subglacial pressure gradients are increasing most rapidly. Between June and July, lags between peak melting and peak tremor amplitude decreased by 3.25 hours. Between June and July, lags between peak melting and peak sliding decreased by 4 hours. These observations likely reflect the removal of the seasonal snowpack as the snowline retreated upglacier as the melt season progressed.

Between July and August lags between peak melting and all other variables decreased. Lags between peak meltwater production and delivery to PIRA moulin decreased by 54 minutes. This change was reflected in the timing of peak moulin water level which occurred 39 minutes earlier in August than in July. Lags between peak melting and peak tremor amplitude decreased by an additional 1.75 hours between July and August, and lags between peak melting and peak sliding speed decreased by one hour.

References

Bartholomaus, T. C., Larsen, C. F., Amundson, J. M., O'Neel, S., Walter, J. I., & West, M. E. (2015). Subglacial discharge at tidewater glaciers revealed by seismic tremor. *Geophysical Research Letters*, *42*, 6391–6398. doi: 10.1002/2015GL064590

Conrad, O., Bechtel, B., Bock, M., Dietrich, H., Fischer, E., Gerlitz, L., ... Böhner, J. (2015). System for Automated Geoscientific Analyses (SAGA) v. 2.1.4. *Geoscientific Model Development*, *8*(7), 1991–2007. doi: 10.5194/gmd-8-1991-2015

Fahnestock, M. A., Truffer, M., SDFE, T. D. A., & Community, U. (2006). *Greenland GNSS Network - KAGA-Kangia North P.S.,.* UNAVCO. doi: 10.7283/FQGY-4535

Gimbert, F., Tsai, V. C., Bartholomaus, T. C., Amundson, J. M., & Walter, J. I. (2016). Subseasonal changes observed in subglacial channel pressure, size, and sediment transport. *Geophysical Research Letters*, *43*(September), 3786–3794. doi: 10.1002/2016GL068337

Herring, T., King, R. W., & McClusky, S. C. (2010). Introduction to GAMIT/GLOBK. *Mass. Inst. of Technol., Cambridge, Mass.*

Kilpatrick, F. A., & Cobb, E. D. (1985). Measurement of discharge using tracers. In *Techniques of water-resources investigations of the united states geological survey* (Vol. Book 3, pp. 1–52).

King, L. A. (2018). *Identifying and characterizing the spatial variability of supraglacial hydrological features on the western Greenland Ice Sheet* (Doctoral dissertation, University of British Columbia). doi: 10.14288/1.0372827

Mejia, J. Z., Gulley, J. D., & Dixon, T. H. (2020). *West Greenland Moulins 2017-2019 Sermeq Avannarleq - GPS/GNSS Observations Dataset.* The GAGE Facility operated by UNAVCO, Inc. doi: 10.7283/VT31-EK40

Mejia, J. Z., Gulley, J. D., Trunz, C., Covington, M. D., Bartholomaus, T. C., Xie, S., & Dixon, T. (2021). Isolated cavities dominate Greenland Ice Sheet dynamic response to lake drainage. *Geophysical Research Letters*, 1–11. doi: 10.1029/2021gl094762

Mejia, J. Z., Trunz, C., Covington, M. D., & Gulley, J. D. (2020). *Meteorological data from two on-ice weather stations at 780 and 950 m asl elevations in the ablation area of Sermeq Avannarleq, West Greenland from 2017-2018.* Arctic Data Center. doi: 10.18739/A2CF9J745

Mejia, J. Z., Trunz, C., Covington, M. D., Gulley, J. D., & Breithaupt, C. (2020). *Moulin hydrological measurements from Sermeq Avannarleq, West Greenland Ice Sheet from 2017-2018.* Arctic Data Center. doi: 10.18739/A2M03XZ13

Pellicciotti, F., Brock, B., Strasser, U., Burlando, P., Funk, M., & Corripio, J. (2005). An enhanced temperature - index glacier melt model including the shortwave radiation balance : development and testing for Haut Glacier d ' Arolla , Switzerland. *Journal of Glaciology*, *51*(175), 573 – 587. doi: 10.3189/172756505781829124

Porter, C., Morin, P., Howat, I., Noh, M.-J., Bates, B., Peterman, K., . . . Nakamura, H. (2018). *ArcticDEM.* Harvard Dataverse. doi: http://doi.org/10.7910/DVN/OHHUKH

Röösli, C., Walter, F., Husen, S., Andrews, L. C., Luthi, M. P., Catania, G. A., & Kissling, E. (2014). Sustained seismic tremors and icequakes detected in the ablation zone of the Greenland ice sheet. *Journal of Glaciology*, *60*(221), 563–575. doi: 10.3189/2014JoG13J210

Smith, L. C., Yang, K., Pitcher, L. H., Overstreet, B. T., Chu, V. W., & Rennermalm, Å. K. (2017). Direct measurements of meltwater runoff on the Greenland ice sheet surface. *Proceedings of the National Academy of Sciences*, *114*(50), 1–10. doi: 10.1073/pnas.1707743114

Trunz, C., Mejia, J., Covington, M., Siegel, V., Conlon, B., & Gulley, J. D. (2021). *Supraglacial stream discharge measurements from six catchments within the Pâqitsoq region of Sermeq Avannarleq, western Greenland Ice Sheet 2017 -2018. Arctic Data Center.* Arctic Data Center. doi: 10.18739/A2D21RK53

Wang, L., & Liu, H. (2006). An efficient method for identifying and filling surface depressions in digital elevation models for hydrologic analysis and modelling. *International Journal of Geographical Information Science*, *20*(2), 193–213. doi: 10.1080/13658810500433453

Xie, S., Law, J., Russell, R., Dixon, T. H., Lembke, C., Malservisi, R., . . . Chen, J. (2019). Seafloor Geodesy in Shallow Water With GPS on an Anchored Spar Buoy. *Journal of Geophysical Research: Solid Earth*, *124*(11), 12116–12140. doi: 10.1029/2019JB018242

Table S1. Catchment geometry

	Low Camp			High Camp	
Name	JEME[†]	PIRA[†]	JNIH	RADI	SBPI
Instrumented	2017	2018	2017	2017	2018
Area (km^2)	0.24	0.24	1.11	16.77	2.37
Length (km)	1.0	1.0	1.8	7.5	1.7
Elongation ratio[‡]	0.55	0.55	1.05	0.62	1.16
Elevation (m.a.s.l.)	779	779	790	947	927
Ice thickness (m)*	503	503	547	634	732
Moulin instrumented	✓	✓		✓	

[†] PIRA and JEME drained the same catchment. PIRA formed during 2018.

[‡] calculated from the catchment's area A and length L following $Re = (A/\pi)^{0.5}/L$.

* Ice thicknesses derived from BedMachine v3 data.

Table S2. Moulin coordinates

	Latitude °N	Longitude (°W)
JEME PIRA	69.4741	49.8232
JNIH	69.4684	49.8318
SBPI	69.5294	49.7231
RADI	69.5428	49.7029

Table S3. Catchment area, discharge, and lags.

	Area	Elevation	Discharge	melt→stage		melt→moulin		melt→sliding	
	km^2	m.a.s.l.	m^3/s	n	LAG hrs	n	lag hrs	n	LAG hrs
`JEME`	0.24	779	0.11	7	2.4±1.6	28	5.2±1.3	20	4.4±1.1
`PIRA`			0.10	3	2.5±1.3	32	4.9±1.5	31	4.8±2.0
`JNIH`	1.11	790	0.14	5	4.2±1.8			7	4.9±1.8
`SBPI`	2.37	927	0.45	3	5.0±1.3				
`RADI`	16.77	947	2.15	11	6.5±1.8	19	7.9±2.2	12	10.5±1.6

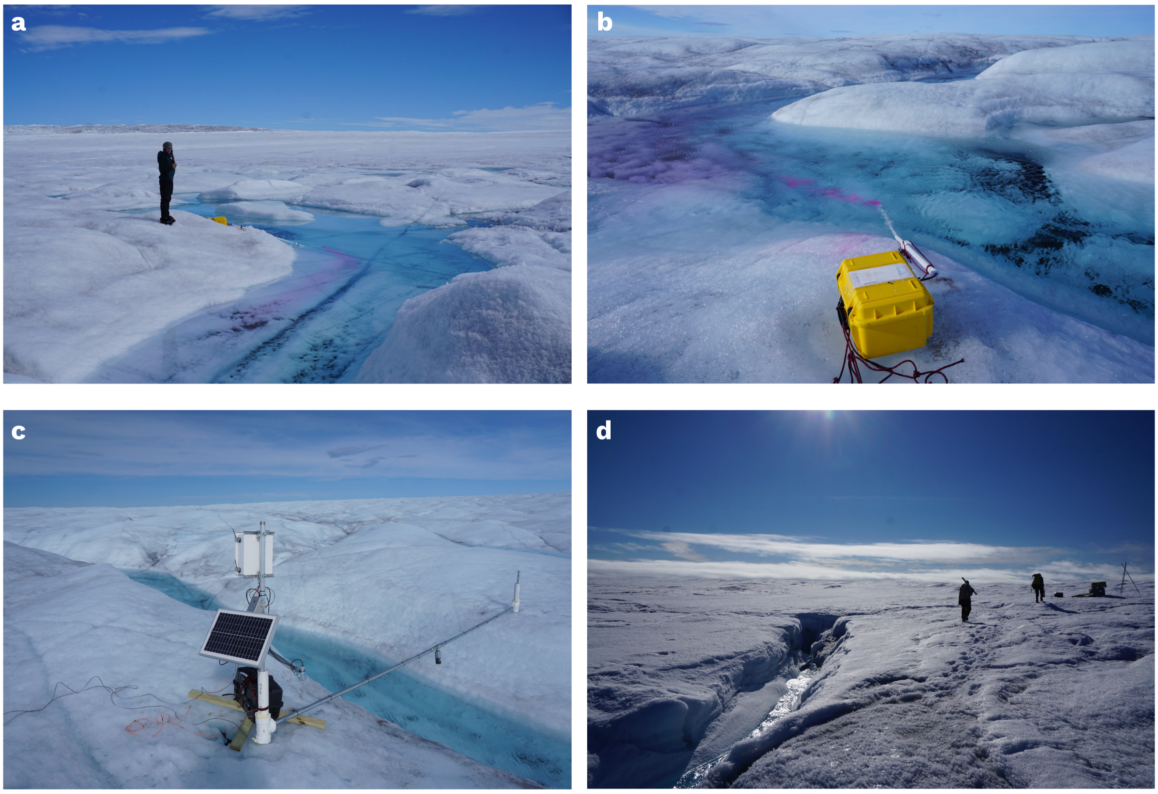

Figure S1. Low Camp supraglacial stream instrumentation. (a–b), Rhodomine dye injection pump positioned several stream widths upstream from our submerged cyclops fluorometer attached to the stream gauging station. (c) Global water WL705-048 ultrasonic water level sensor attached to a self-lowering cross-bar. The instrument was powered by a 12V battery, recharged with a solar panel, also powering the Campbell scientific data logger which recorded stage measurements every 15-minutes. Another ultrasonic range sensor was mounted to a small crossbar near the data logger, positioned downward to measure surface ablation. (d) JNIH moulin, instrumented with a Geokon 4500HD piezometer.

Figure S2. High Camp supraglacial stream instrumentation. (a) Radical (RADI) moulin, instrumented with a Geokon piezometer in mid-July 2017. (b) RADI stream gauging station. Stream stage was measured using the same setup deployed at our Low Camp field sites where a Global Water ultrasonic water level sensor (WL705-012) measured stream stage at 15 minute intervals.

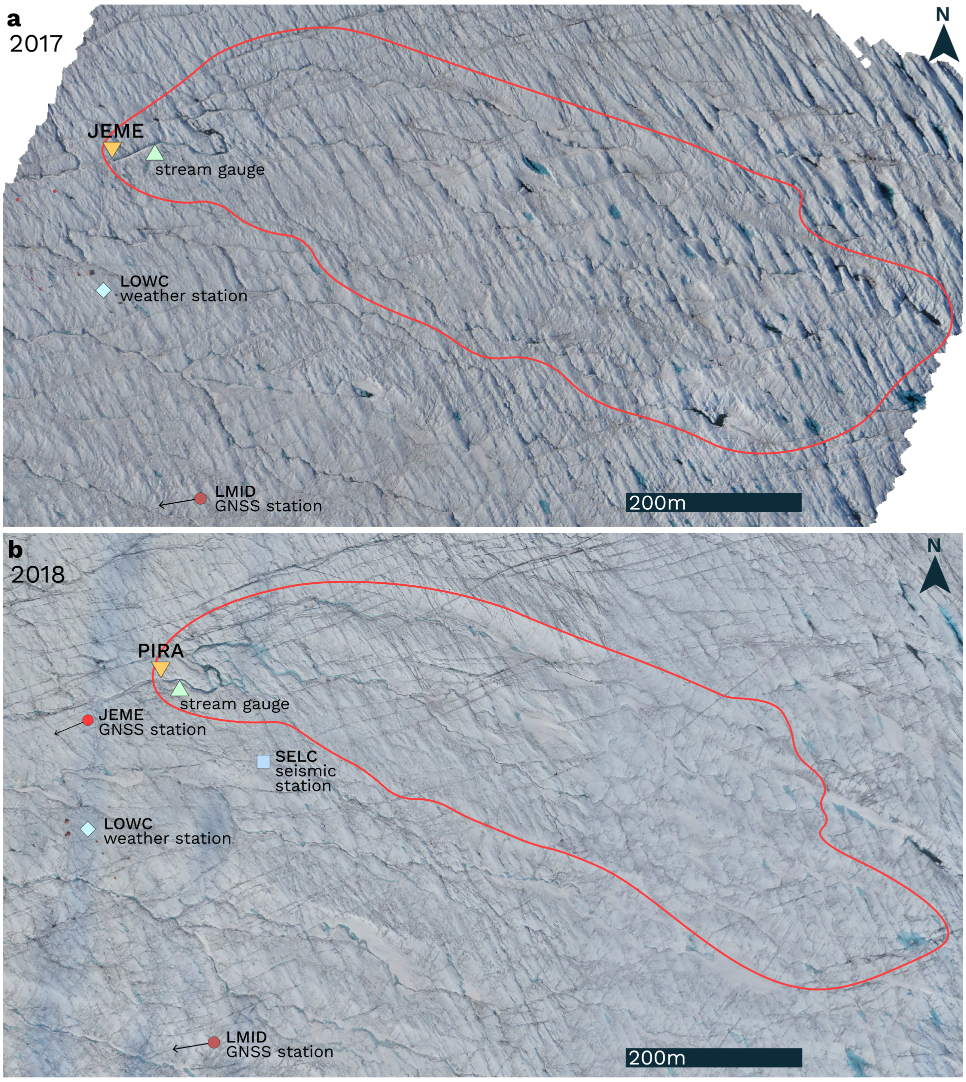

Figure S3. JEME and PIRA moulin and drainage basin comparison. (a), Drone orthoimage from July 2017 showing the location of our instrumented moulin JEME and the bounds of its supraglacial drainage basin. (b) Drone orthoimage from July 2018 showing the location of our instrumented moulin PIRA which opened in the same location as JEME the previous year. The drainage basin is delineated and other instruments are shown along with the ice flow direction in the area (black arrows).

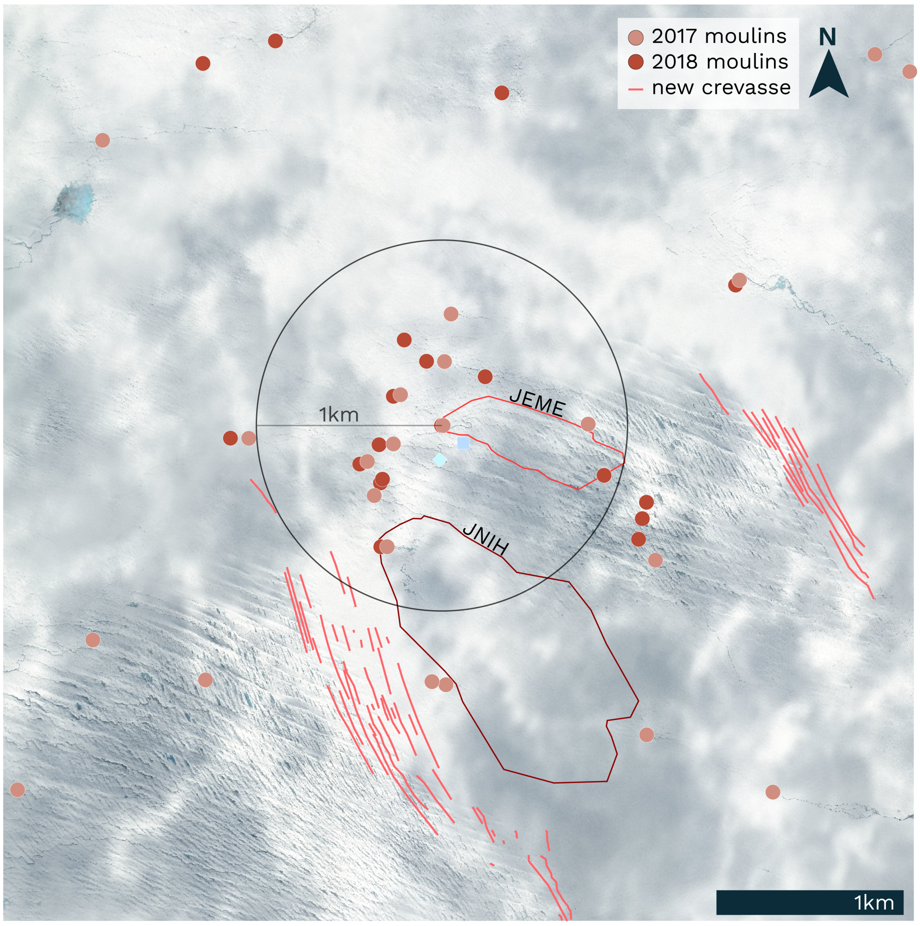

Figure S4. Low Camp moulin and crevasse distribution. WorldView-2 Imagery (copyright 2017 DigitalGlobe Inc.) acquired 03 July 2017. Moulins identified in 2017 (orange) and 2018 (red) are marked by circles. Red lines show newly formed crevasses. JEME and JNIH drainage basins and terminal moulins are also marked and labeled. An area with a 1-km radius centered on JEME/PIRA moulin is shown, representing a diameter of approximately four ice-thicknesses.

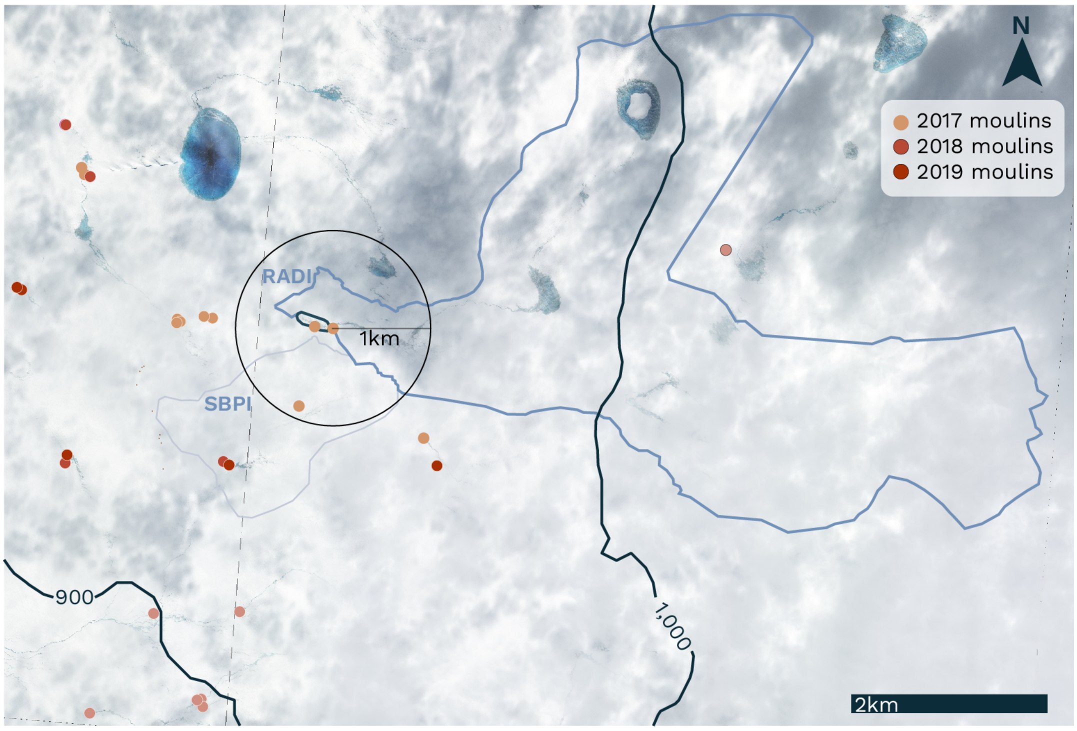

Figure S5. High Camp moulin and crevasse distribution. WorldView-2 Imagery (copyright 2017 DigitalGlobe Inc.) acquired 03 July 2017. Moulins identified in 2017 (orange) and 2018 (red) are marked by circles (2019 darkest). RADI drainage basin, along with SBPI and a small nearby moulin and drainage area are delineated. An area with a 1km radius is centered on RADI moulin, with the diameter representing approximately three ice thicknesses.

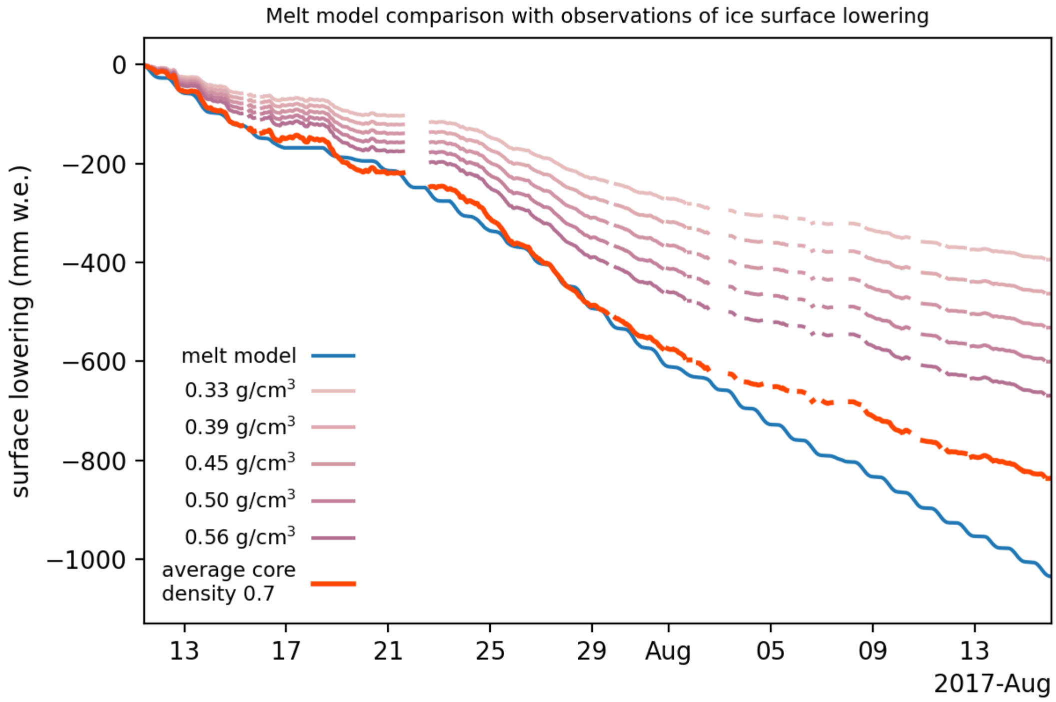

Figure S6. Observed and calculated surface meltwater production comparison for Low Camp, 2017. Modeled surface meltwater production (blue) compared with ice surface ablation measurements converted to mm w.e. using average ice densities ranging from 0.33–0.56 g/cm^3 in purple and the best fit of 0.7 g/cm^3 in red.

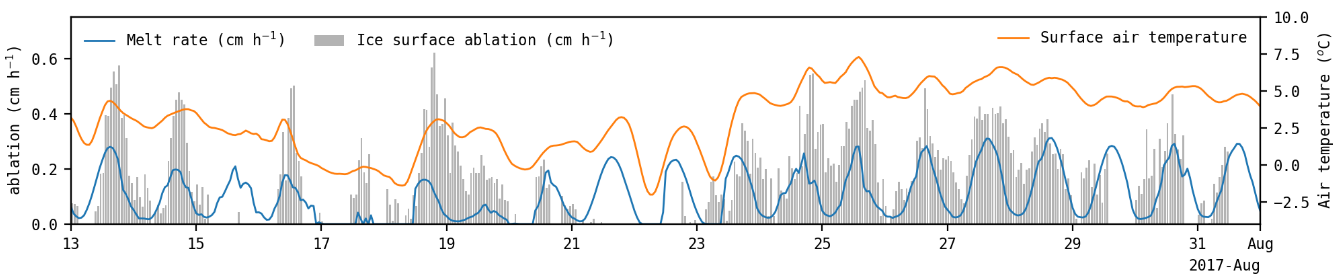

Figure S7. Comparison between hourly surface air temperature (orange), melt rate (blue), and ice surface ablation (gray) recorded at Low Camp during July 2017.

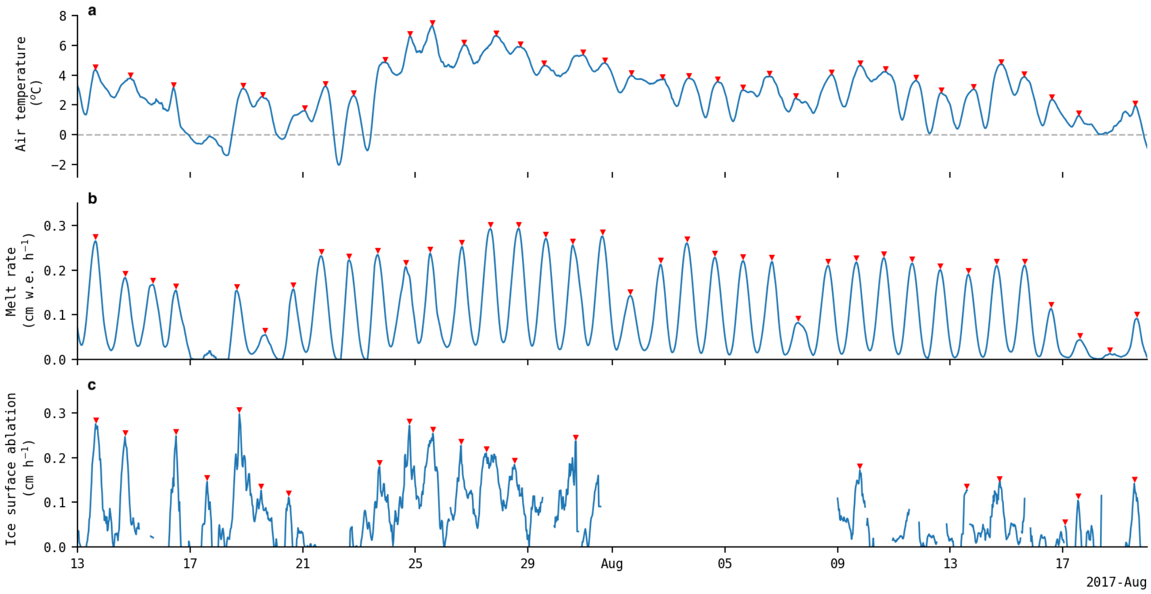

Figure S8. Comparison between diurnal extrema in meteorological measurements from Low Camp, 2017. (a) Surface air temperature measured by LOWC AWS positioned at Low Camp. Diurnal extrema picks used to calculate the average timing of peaks is marked by red triangles. Peak air temperature occurs on average at 15:30±3.3 hours with n = 35. (b) Calculated melt rate determined using meteorological measurements from LOWC AWS. Diurnal peak melt rate occurs at 13:30±1.0 hours where n = 37. (c) Hourly ice surface ablation measured at the JEME gauging station at Low Camp in 2017. A two hour smoothing window is applied and we ignore dates where our instrument did not capture the entire range of diurnal variability. Peak ice surface ablation occurred on average at 13:30±3.4 hours where n = 20.

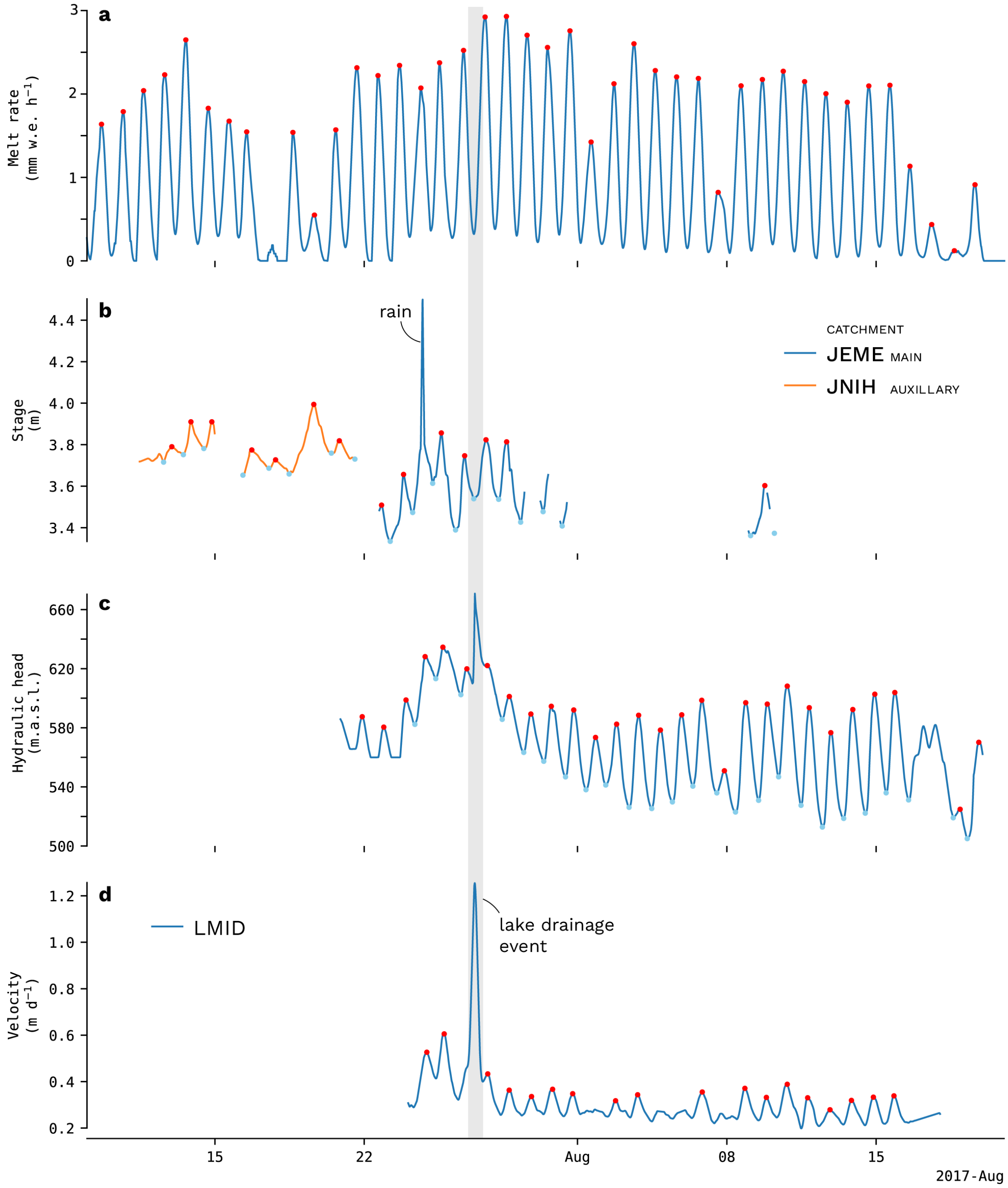

Figure S9. Low Camp 2017 timeseries and extrema picks. (a) Melt rate with diurnal maxima marked in red. (b) Supraglacial stream stage for our auxiliary catchment JNIH (orange) and our main catchment JEME (blue). Diurnal maxima (red) and minima (light blue) are marked. The abrupt jump in stream stage corresponds to a rain event. Stream stage is determined from an arbitrary reference point due to lack of a continuous stream depth timeseries. (c) JEME moulin hydraulic head. Flat minima values on 21-23 July were caused by moulin water level dropping below the piezometer's submerged depth. Continued lowering on 24 July 2017 enabled measurements of the full range of diurnal variability. (d) Along-flow surface ice velocity from the LMID GNSS station. Gray shading marks the timeperiod associated with a rapid supraglacial lake drainage several kilometers upglacier of our study site (see Mejia et al., 2021, for a complete description of this event).

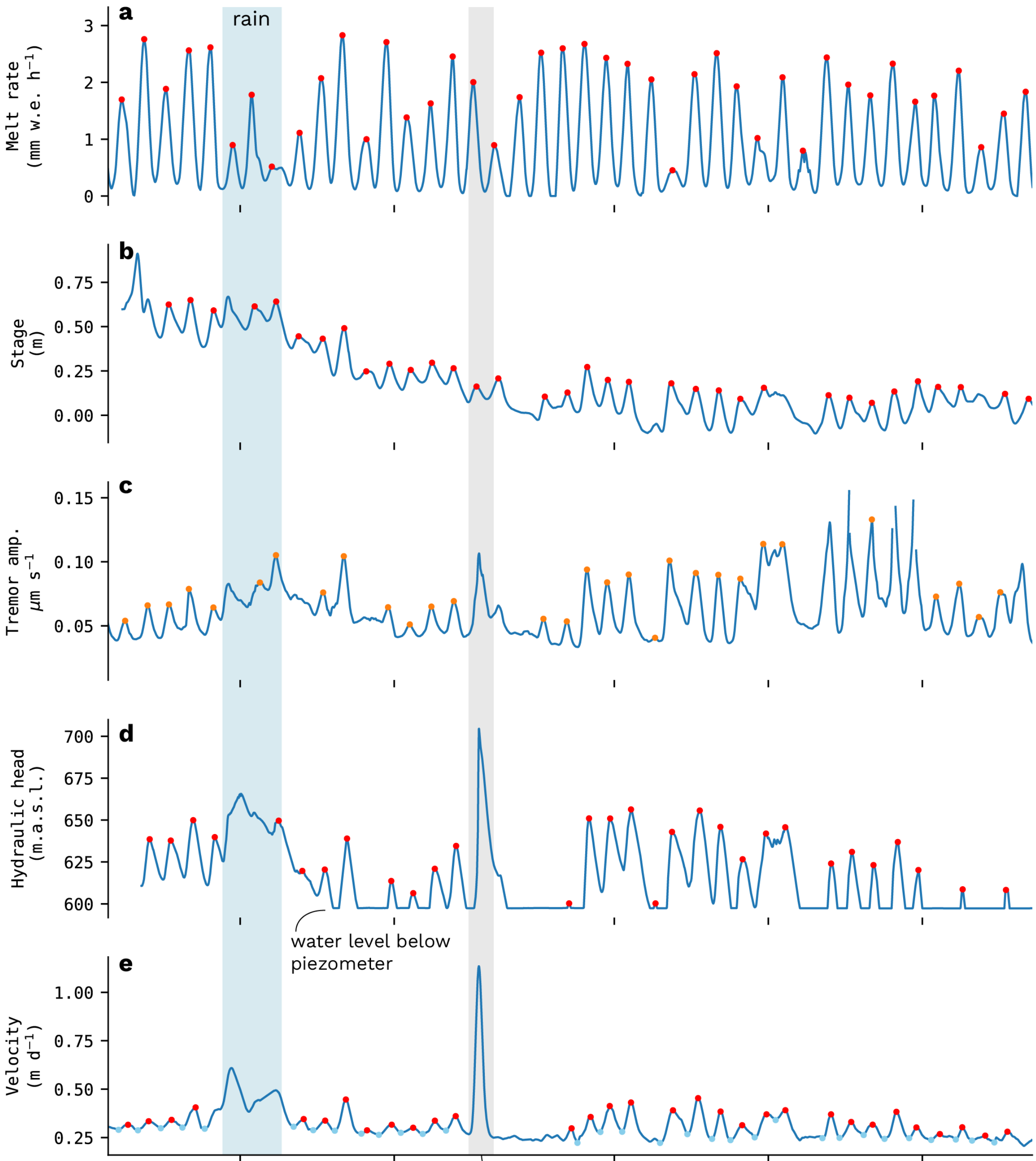

Figure S10. Low Camp 2018 timeseries and extrema picks. Similar to Figure S6 but for the 2018 melt season. (a) Surface melt rate with extrema picks. (b) PIRA stream stage. (c) PIRA hydraulic head. The flat lines mark the piezometer's elevation within the moulin shaft and indicate water levels dropping below the sensor. (d) Along-flow ice velocity from station LMID. Spikes in panels c–e on 25 July are a result of a subglacial flood-wave passing beneath our site (see Mejia et al., 2021, for a complete description of this event).

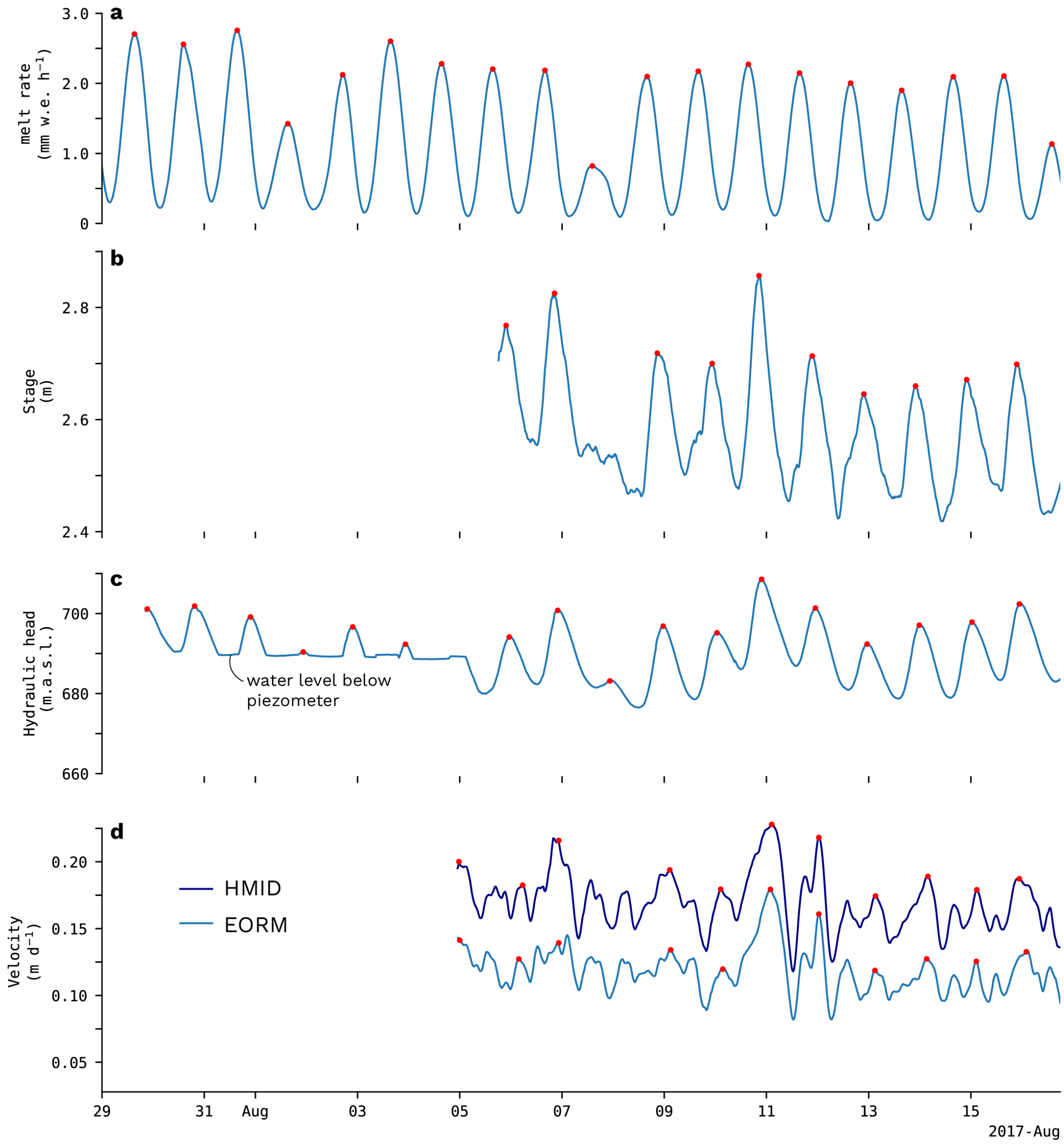

Figure S11. High Camp 2017 timeseries and extrema picks. (a) Melt rate with diurnal peaks (red). (b) Radical River supraglacial stream stage with respect to an arbitrary datum of 4 m. (c) Radical Moulin hydraulic head. The full range of diurnal moulin head oscillations was captured after the further lowering of the piezometer within RADI moulin on 5 August. (d) Along-flow ice velocity measured from stations HMID (purple) and EORM (blue). Diurnal peaks in ice velocity were confirmed with visual inspection of displacement timeseries.

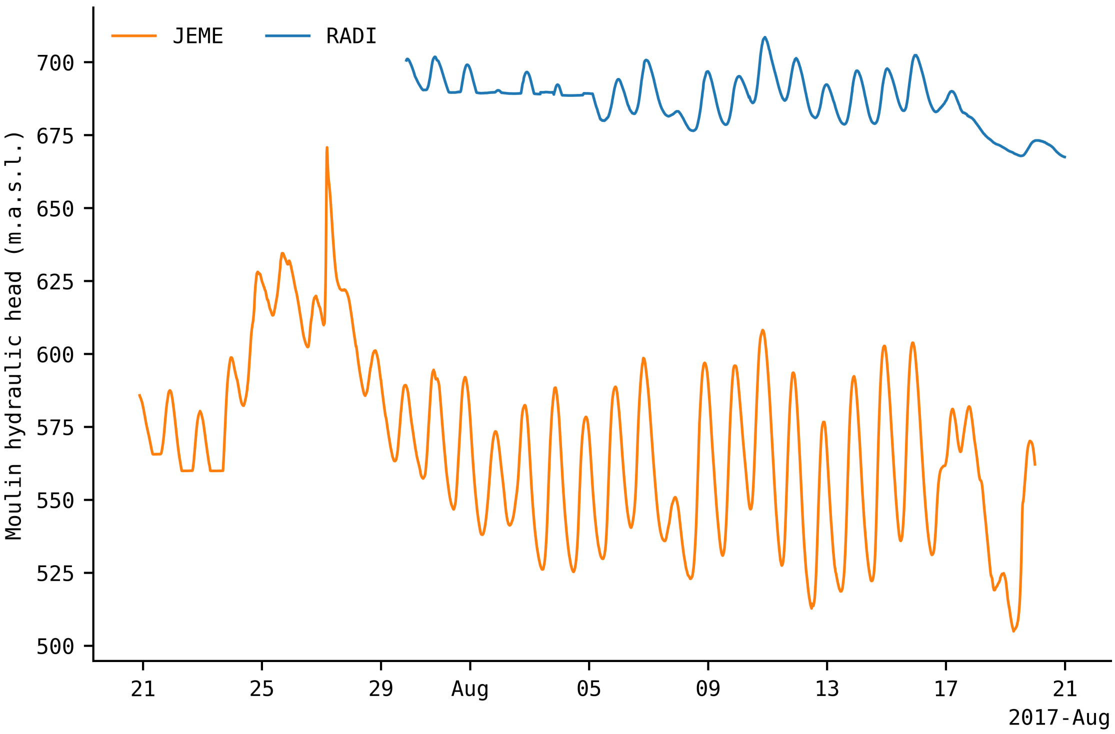

Figure S12. Moulin water level comparison. Measurements from Low Camp's JEME moulin (orange) and High Camp's RADI moulin (blue) plotted together on the same axis. The ice surface at Low Camp is 765.8 m.a.s.l. and the ice is approximately 503 m thick. The ice surface at High Camp is 933.2 m.a.s.l. and the ice is approximately 712 m thick.

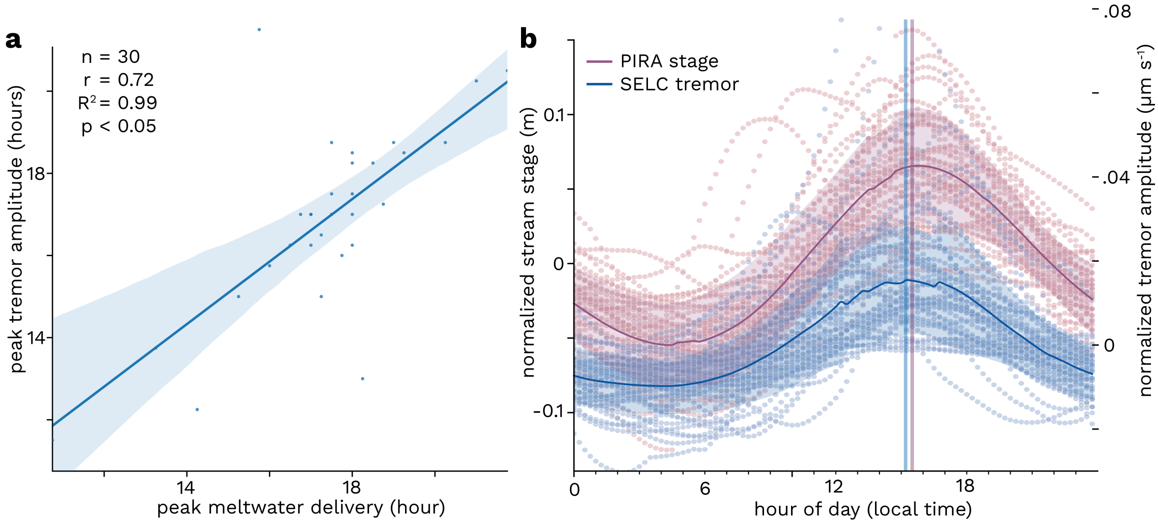

Figure S13. Glacio-hydraulic tremor and meltwater delivery relationship, Low Camp 2018. (a) Peak timing correlation between the time (decimal hours) of peak meltwater delivery to moulin PIRA, and the time of peak tremor amplitude. Blue line shows a linear regression between the two values with the standard deviation confidence interval shaded in blue. Annotations describe ordinary least squares correlation R^2=0.99 and p-value < 0.05 and the Pearson correlation coefficient (r=0.72). (b) Normalized diurnal fluctuations for stream stage (purple, left axis) and tremor amplitude (blue, right axis). Average values and the associated standard deviation from the mean are plotted, with the average peak meltwater delivery (15:30 UTC-02:00), and peak tremor amplitude (15:15 UTC-02:00) indicated with vertical lines.

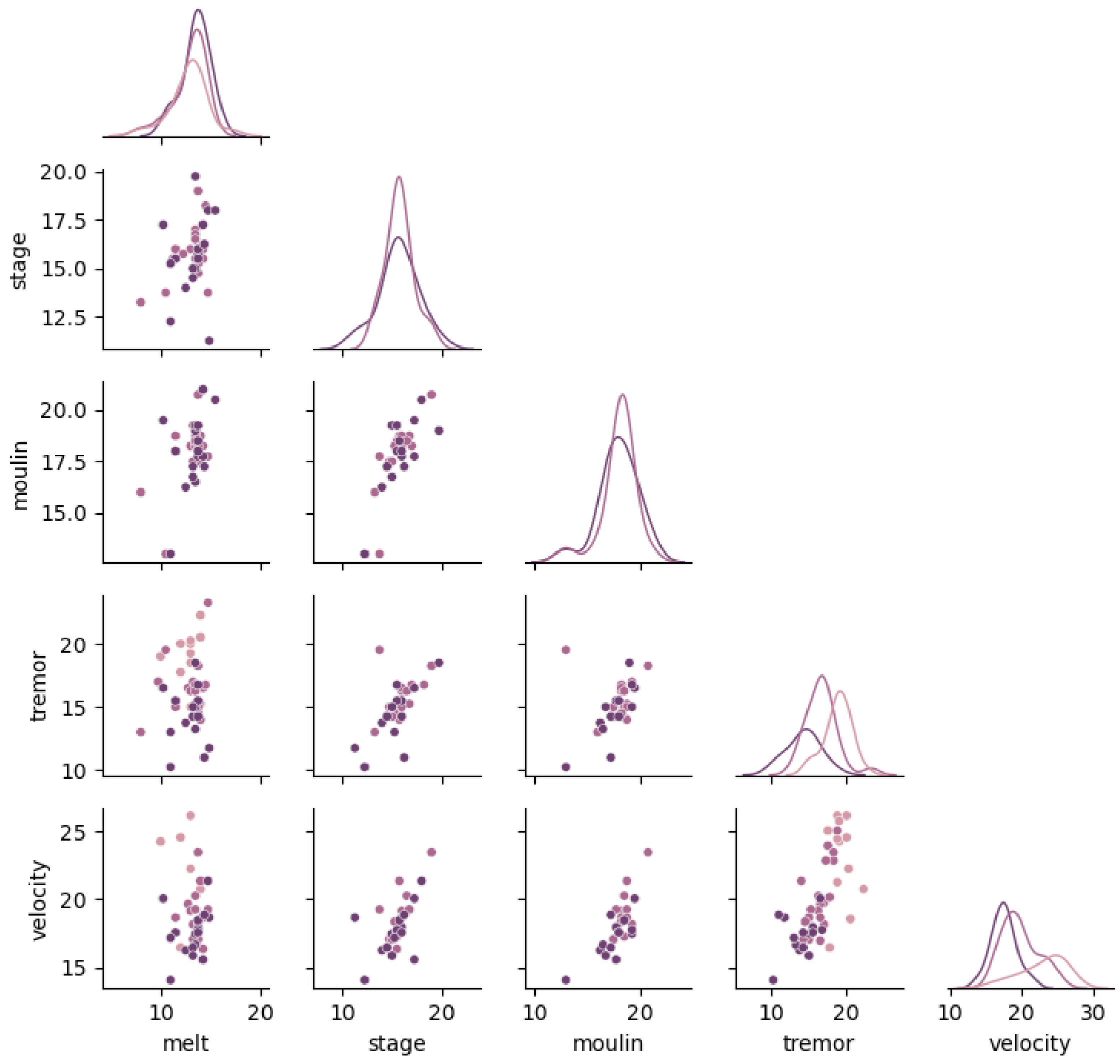

Figure S14. Low Camp 2018, correlation between variables and monthly comparison. Colors correspond to values from June (pink), July (light purple), and August (purple).